1-1-2011

Second generation of the diagnostic tool for the In vivo measurement of strontium levels in human bone

Mira Sibai
Ryerson University

Second Generation of the Diagnostic Tool for the *In vivo* Measurement of Strontium Levels in Human Bone

By
Mira Sibai
Honours of B.Sc. Université Libanaise, 2008
Beirut, Lebanon

A thesis

presented to Ryerson University

in partial fulfillment of the

requirements for the degree of

Master of Science

in the Program of

Biomedical Physics

Toronto, Ontario, Canada, 2011

Author's Declaration

I hereby declare that I am the sole author of this thesis.
I authorize Ryerson University to lend this thesis to other institutions or individuals for the purpose of scholarly research.

_____

Mira Sibai

I further authorize Ryerson University to reproduce this thesis by photocopying or by other means, in total or in part, at the request of other institutions or individuals for the purpose of scholarly research.

_____

Mira Sibai

Abstract

"Second Generation of the Diagnostic Tool for the *In vivo* Measurement of Strontium Levels in Human Bone". Mira Sibai, M. Sc. Biomedical Physics, Ryerson University, Toronto, 2011.

Strontium (Sr) is an element collected naturally in the human body through diet. It has a paradoxical effect on bone health, where at low doses Sr enhances bone health. The beneficial effects of Sr warranted its use as a complimentary treatment for osteoporosis. The current source-based Sr *in vivo* x-ray fluorescence (IVXRF) system is in clinical use to study the incorporation and retention of Sr in bone after administration of Sr supplements. This system however can only monitor relative changes in bone with a limited level of accuracy. Therefore a second generation of the diagnostic tool has been developed and optimized aiming to improve the accuracy and precision of an IVXRF measurement. The system comprises of an optically focused x-ray tube producing monochromatic x-rays and a silicon drift detector. Furthermore, optimal parameters to run the system are investigated, along with three different means of signal normalization.

Acknowledgements

Throughout the two years at Ryerson, I have learnt to live through the excitement and joy of research with a few visits through frustration and hardship, teaching me diligence and patience. I have been fortunate to always find an open hand on the other side and I am grateful to have a chance to greatly thank them.

Firstly to my mentor, advisor, source of inspiration and motivation, Dr. Pejović-Milić ; I cannot thank you enough for believing in me from day one. Your endless passion, guidance, and encouragement have been the source of my ongoing energy toward this project. I am most fortunate to have had a chance to work with you as I am most grateful for your endless support and precious advice on various issues, academic and non-academic. You have never failed to find time to answer my endless questions, thank you.

Secondly to whom I consider my second supervisor, Dr. Chettle; In spite of your very tight schedule, you somehow always had time for me to come to your office and ask you a “few” questions here and there. From every one hour meeting we had, I learned what would take me a few days to learn. I was not fortunate enough to learn your talent in mental calculations. Your input and questioning of my results have been extremely valuable in the final analysis and conclusion of this work.

I wish to express my thanks to my third committee member, Dr. Ford, who has managed to always be flexible on the venue of my committee meetings, which often took place outside of Toronto. Your dedication, support, and your input in this work is greatly appreciated.

To Elstan Desouza, graduate student and colleagueat McMaster University; you made everything much easier to understand and accomplish. Thank you dearly for your patience and assistance. You have shown me the joy of testing theory by experimentation. From you, I have learnt the importance of consistency, accuracy and precision, which turn to be the main keywords of this thesis! I mostly enjoyed the times we would discuss things and bounce ideas off one another, many thanks…

To the technical support at the Tandem accelerator at McMaster University, for facilitating my experiments as much as possible. To my fellow colleague and friend Helen Moise, I am endlessly grateful for your assistance and companion at McMaster.

I extend my gratitude to the physics administrative staff, especially Tesse Sy, who has always been patient and happy to help me. To the faculty members at Ryerson, your doors are always open for us to seek guidance. In particular, I thank Dr. Heath and Dr. Kolios for your valuable suggestions and advice.

Last but definitely not the least, my gratitude and love goes to my friends, who have all helped me to make my experience at Ryerson, a memorable one. Thank you!

Table of Contents

List of Tables

TABLE OF FIGURES

Chapter 1 Introduction

1.1 Strontium and Strontium Metabolism

Strontium (Sr) is one of the alkaline earth metals discovered near a Scottish village Strontian in 1970. It has a high affinity to oxygen and thus never occurs free in nature. Two common compounds of Sr oxides are the celesite ($SrSO_3$) and strontianite ($SrCO_3$) (Nielson, 2004). Natural Sr comprises of four stable isotopes: Sr-84, Sr-86, Sr-87, and Sr-88 with natural abundances of 0.56%, 9.86%, 7.02% and 82.56% respectively (Nielson, 2004).

Sr makes 0.02-0.03% of the earth's crust as opposed to the 3.63% Ca makes (Turekian and Wedepohl, 1959). The average amount of Sr/Ca ratio in bone of a reference man is estimated to be 32µg/g Ca (ICRP 1975). Sr is not an essential element, but rather considered a minor element (Nielson, 2004). Comar and colleagues showed that Sr/Ca ratios in tissues and body fluids corresponded directly to Sr/Ca ratios in diet, where leafy vegetables, cereals, grains, and seafood are all examples of Sr rich foods (Comar *et al*., 1956). In fact, since Sr initially present in soil is retained in plants, dietary Sr levels are correlated to one's geographical location, where plants rooted in different soils will result in different plant Sr levels (Turekian and Kulp, 1956).

According to the International Commission on Radiological Protection's (ICRP) biokinetic model of radionuclide intakes, once ingested, radioactive-strontium is readily absorbed in the gastrointestinal (GI) tract and retains there for a biological half-life of 30 years, causing radiogenic effects and bone deformities (ICRP 1993). Because Sr has similar physiochemical properties to Ca, Sr competes with Ca in the assimilation, excretion and absorption pathways. In general, Sr absorption in the GI tract increases under fasting conditions and in the presence of vitamin D, but decreases in the presence of Ca (Nielson, 2004). Although plants' retain Ca and Sr in a similar manner, Sr/Ca ratios decrease appreciably once Sr is ingested by animals or humans (Comar *et al*., 1957). The discrimination of the GI tract of Sr in favor of Ca is explained to be due to the larger atomic size of Sr compared to Ca. Similar to Ca, Sr forms divalent

cations in biological fluids such as serum and plasma, where the degree of protein binding of Sr in biological fluids is in the same order of magnitude as that of Ca (Nielson, 2004). Both minerals are bone seeking elements where in animals, 99.1% of Sr is retained in the bone as opposed to 98.6% in the case of Ca (Nielson, 2004).

The aforementioned physiochemical similarities of Sr and Ca have been exploited in diagnostic and therapeutic applications. For example, radioactive Sr-85 has been used as a biomarker for Ca in biokinetic studies, while radioactive Sr-89 has been used to treat bone pain due to metastases from prostate and breast cancer (Robinson *et al.,* 1989). Using radioactive Sr to monitor Ca in the body can be misleading due to some differences in the body's response to either element. Sr for instance is not homeostatically controlled as the body does not actively regulate Sr levels within the cells, while Ca is under homeostatic control (Nielson, 2004).

1.2 Strontium's Beneficial and Deleterious Effect on Bone

The effects of Sr on bone could be clustered in two groups. One group of studies demonstrated that Sr causes hypomineralization and enhanced bone resorption, while the second group of studies demonstrated that Sr can increase bone mass, bone cell replication and bone mineralization (Verberckmoes *et al.,* 2003). The two groups appear to be contradictory at first glance, yet a closer look at the two clustered groups show that Sr's effect on bone is dose dependent. Studies on the deleterious effect of Sr on bone corresponded to high Sr levels (Cabrera *et al.,* 1999; Özgür *et al*., 1996), while studies on the favorable effect of Sr bone corresponded to low doses of Sr (Grynpas *et al*., 1996; Reginster *et al*., 2005).

Shorr and Carter were probably the first to recognize the therapeutic effect of Sr on bone (Shorr and Carter, 1952). Seven years later, Sr lactate was used to reduce bone pain in osteoporotic patients (McCaslin *et al*., 1959). The possible therapeutic effects of bone Sr were overshadowed at that time after radioactive Sr-90 was widely dispersed in the fallout from atmospheric testing of nuclear weapons (Cabrera *et al.,* 1999). Later in the 1980s, Sprague-Dawley rats once injected by $SrCl_2$ were found to have increased bone formation even at a faster rate than the second group of rats which were injected with $CaCl_2$, but for a shorter duration (Ferraro *et al.*, 1983). Bone histomorphemetry and biomechanical examinations of rats' skeletons showed that a low dose strontium regime, in the form of $SrCl_2$ in drinking water, reduced bone resorption and increased trabecular bone volume with an augmentation of bone mass, without any changes in bone mineralization (Marie *et al*., 1985). More so, when healthy rats were

fed with a synthetic diet that included 0.2% Sr added in their drinking water, an increase in bone forming surface and bone mineral volume, with no difference in the mineral profile as compared to the control group having no Sr in their diet was observed (Grynpas *et al.,* 1996). An administered dose of Sr ranelate (Protelos®) from 0.39 to 2.91 mmol Sr/Kg/day given to healthy adult monkeys confirmed the results of increased bone mass and volume with no deterioration in bone crystal matrix observed from the previous *in vivo* studies (Buehler *et al*., 2001).

Osteoporosis is widely known as a bone disease affecting one in four women over fifty years of age and one in eight men in the same age group (WHO, 1994). It is characterized by reduced bone mass and deteriorated bone tissue leading to increased bone fragility and higher risk of fracture, particularly in the hip, spine and wrist. WHO classifies an individual as osteoporotic or osteopenic based on the obtained bone mineral density (BMD) measured by Dual Energy X-ray Absorptionmetry (DEXA). Osteoporosis is defined as a bone density T score at or below 2.5 standard deviations (T score) below the normal peak values for young adults. On the other hand, osteopenia is defined as a bone density T score between -1 and -2.49 (WHO 1994). WHO, however, takes bone density as the sole factor to determine osteoporosis, and thus ignores bone quality and tissue connectivity that may enhance the disease.

An effective treatment for osteoporosis should enhance bone strength by improving bone geometry, cortical thickness, trabecular bone morphology, and intrinsic bone tissue quality. This is achieved by a healthy balance between bone formation mediated by bone forming-cells, or osteoblasts, on one side and bone resorption mediated by bone resorbing cells, the osteoclasts, on the other side (Riggs *et al.,* 2005). Since bone decomposition is much faster than bone formation in osteoporotic patients, treatments may target one side of the balance and not the other. In general, treatments for osteoporosis can be divided into three major groups (Riggs *et al*., 2005):

1- Anti-destructive or anti-catabolic therapy, which aims to decrease bone decomposition.
2- Anabolic therapy, which consists of anabolic drugs used to enhance bone formation.
3- Combined therapy, which requires the use of a catabolic drug for a maximum period of 24 months followed by the use of an anabolic drug.

Strontium ranelate, is a combined therapy medication that has been proven to enhance bone health and decrease the risk of fracture (Fonseca, 2008). An analysis of the role of strontium ranelate on

rebalancing bone turnover is well documented in the literature (Meunier *et al.,* 2004; Reginster *et al.,* 2005; Fonseca, 2008).

On a cellular level, bone is composed of cells and an extracellular matrix, collagen type 1, which directs Ca deposition in the hydroxyapatite crystal. Since Sr is a divalent cation like Ca, it can activate the calcium-sensing receptor (Ca-R) expressed on pre-osteoblasts, and thus increases these cell's differentiation and activity, leading to the synthesis of collagen type 1 and mineralization (Fonseca, 2008). Interestingly enough, Ca-R also affects osteoclast differentiation, along with osteoclast apoptosis (Fonseca, 2008). These findings suggest that strontium ranelate effects bone strength at a cellular level, and this effect is mediated through enhanced activation of Ca-sensing receptors.

On a macroscopic scale, two randomized double blinded clinical trials have verified the therapeutic action of low dose Sr on bone mineralization and on the risk of fracture to date; they are the SOTI (Spinal Osteoporosis Therapeutic Intervention) and the TROPOS (Treatment of Peripheral Osteoporosis) studies (Meunier *et al.,*2009; Reginster *et al*., 2008) . The SOTI study tested the efficacy of 2g/day Sr ranelate administered to postmenopausal women with osteoporosis against vertebral fractures; while TROPOS tested the efficacy of Sr ranelate on preventing non-vertebral fractures in postmenopausal osteoporotic women, which both were extended over a period of five years. The two studies showed a significant decrease in fracture risk (15%-39%) and an increase in BMD values at the lumbar spine (15%), femoral neck (7.1%), and at the hip (9.8%). Moreover, it was observed that the women under Sr ranelate supplementation had less back pain than the women in the placebo group. The two year extension from the original study also indicated that when women stopped taking strontium ranelate, the BMD values decreased quickly. The authors explain this decrease due to the clearance of strontium from bone and due to the additional artificial increase in the recorded BMD values caused by the presence of strontium in bone. In fact, Meunier and colleagues (2009) predict the overestimated BMD values can mount to 50% of its actual value.

In contrast, high doses of strontium have been reported to produce deleterious effects on bones, especially if calcium intake is low. This seems to be caused by impaired intestinal absorption of calcium and reduced renal production of 1,25-dihydroxycholecalciferol, the metabolically active form of vitamin D in the intestine (Verberckmoes *et al*., 2003). In addition, it has been suggested that Sr blocks the biosynthesis of 1,25-dihydroxycholecalciferol inducing thus bone malformations (Verberckmoes *et al*., 2003). Verberckmoes and colleagues (2003) explain such distortion of the bone matrix due to the larger Sr radius, which in turn expands the lattice, and thus weakens bone structure.

High doses of Sr seem to induce rickets due to an impaired metabolism of vitamin D and calcium, while high doses of Sr induce osteomalacia in the elderly (Özgür *et al*., 1996; Cabrera *et al*., 1999). In one study, the prevalence of rickets in a Sr-rich soil region, was much higher than in a region, which did not have a high concentration of Sr in its soil (31.5% vs. 19.5%) (Özgür *et al*., 1996). In another study, a correlation between osteomalacia and high bone Sr concentrations in dialysis patients was found (Cabrera *et al*., 1998). Overall, it is evident that Sr has a dual, beneficial and deleterious, effect on bone that is dose dependent.

1.3 Measuring Bone Sr *In Vivo* Non-Invasively

The main non-invasive techniques capable of measuring bone Sr non-invasively are Neutron Activation Analysis (NAA), dual photon absorptiometry (DPA), and X-ray Fluorescence (XRF). DPA and XRF are based on photon interaction with tissue, and NAA is based on neutron interactions; nevertheless, each technique extracts elemental concentrations rather differently.

Neutron Activation Analysis (NAA) involves a source of neutrons bombarding a sample in order to excite targeted isotopes via neutron capture of thermal neutrons or inelastic scattering of fast neutrons. The excited nuclei then emit ϒ photons, which are counted and are then correlated to the concentration of the element of interest. This method of counting is referred to as prompt NAA. Nitrogen and Cadmium are examples of elements measured using this method (Sutcliffe *et al.,* 1996). Alternatively, the excited nucleus may de-excite to a radioactive daughter nucleus followed by a delayed ϒ photon, which is detected and used to find elemental concentration. This method of the delayed ϒ photon detection is referred to as delayed NAA (Sutcliffe *et al.,* 1996). Aluminum, manganese, calcium and fluorine all haven been reported to be successfully measured using delayed NAA (Sutcliffe *et al*., 1996*).* Regardless of the counting method, the main advantage of *in vivo* NAA is that neutrons and gamma ray sources have relatively good penetrating depths, and thus can be applied to deep seated organs. Therefore, for estimating bone Sr, NAA can sample the whole irradiated bone. Furthermore, it is possible to determine simultaneously the Ca and Sr content, which are each distinguished by the kinetic energy of their emitted ϒ photons. This is advantageous over x-ray techniques because Ca x-rays of energy 3.4 keV are heavily attenuated through skin and are thus not detected. Obtaining Sr/Ca ratio is more clinically relevant than absolute values of Sr, because both have similar physiochemical properties as discussed in section 1.1, and because the ratio is indicative of one's dietary habits (Hult and Fessler, 1998). On the other hand, *in vivo* NAA is limited to elements that only have high neutron capture cross

sections. More so, the gamma ray spectrum from humans is rather complex, where other elements are activated creating gamma photons that may interfere with the photons of interest (Byun *et al.,* 2007). Neutron sources are also difficult to house for radioprotection purposes (Sutcliffe *et al*., 1996). Nevertheless, the major limitation is the dose delivered to the whole body which can mount to 10 mSv (Byun *et al.,* 2007). This is put into perspective as the annual dose limit in North America is 3 mSv. For the case of Sr NAA measurement, it has been reported that NAA is highly sensitive in measuring Sr from the nuclear reaction of ^{88}Sr (n, 2n) ^{87mSr} with a neutron cross section σ=220mb at neutron energy 14 MeV (Hult and Fessler, 1998) or from the nuclear reaction of ^{86}Sr (n,ϒ)^{87m}Sr (Zaichick, 2004), which however is inefficient, as the natural abundance of ^{86}Sr is only 9.86%. However, the half-life corresponding to the previous two reactions is 2.8 hours, and thus long detection times are required, which are not practical for *in vivo* measurements.

Dual Photon Absorptiometry (DPA) is based on the transmission of photons through soft tissue and bone, where the relative amount of Sr in the hydroxyapatite crystal is determined by exploiting the difference in attenuation of Ca and Sr at the photon energies 59.8 keV and 365 keV emitted by the radioisotopes Am and Ba respectively (Webber, 2006). Similar to NAA, it can measure Sr and Ca simultaneously, as well as sample the whole measurement site. It has not been further developed for *in vivo* bone Sr due the following reasons:

1) DPA relies on the assumption that the measured object consists of only two radiologically distinct materials, which is not realistic as both soft tissue and bone alone vary in composition from one measurement site to another (Webber, 2006).

2) In order to determine analytically the amount of Ca and Sr present in the measured site, the measured body part should be immersed in a water bath, by which it is assumed that water has the same attenuation properties as soft tissue (Zamburlini *et al*., 2008),

3) The most important limitation for *in vivo* bone Sr analysis using DPA is its lack of sensitivity to detect Sr levels from individuals not treated with Sr supplements (Nielson *et al*., 2004).

X-ray Fluorescence (XRF) is based on the fluorescence of x-rays from a sample when incident photons interact with the sample via the photoelectric effect. *In vivo* X-ray Fluorescence (IVXRF) refers to the same phenomenon, except XRF is applied *in vivo* and not to an excised organ.

When an incident x-ray photon strikes a sample, it is either scattered (Compton or coherent scattering) or is absorbed (photoelectric effect) by atoms in the sample. Compton (or incoherent scattering) is the inelastic scattering of the incoming photon by an electron in a valence shell. The Compton photon thus loses part of its initial energy and is scattered with energy E as shown below:

$$E = \frac{h\vartheta}{1+\frac{h\vartheta}{m_e c^2}(1-cos\theta)} \quad (1)$$

where Θ is the angle between the incident photon and the scattered photon, $h\vartheta$ is the photon's incident energy, and $m_e c^2$ is the electron's rest mass.

In the case of coherent scattering, the photon interacts with the whole atom causing it to vibrate and re-emit the photon with no energy loss. Because coherent photons reach a detector with no energy loss, the area under the corresponding photopeak is indicative of the experimental conditions such as the source activity, sample size, geometry, and subject or phantom positioning. The process by which an x-ray is absorbed completely by a tightly bound electron is called the photoelectric effect. If the x-rays have energies above the absorption edge of an orbital shell i.e. just above the binding energy of the orbital shell, an electron can either be excited or ejected, thus creating a vacancy. Creation of a vacancy allows an electron from an outer shell to de-excite to a lower energy shell, leading to the emission of fluorescent x-rays or to the emission of an Auger electron from a higher energy level. The fluorescent x-rays are characteristic to each element as they have energies equal to the difference between the binding energies of the two shells allowing the non-invasive measurement of elemental concentration in a given sample. The closer the energy of the incident x-ray is to the absorption edge of a certain shell, the higher the absorption probability. The probability of ejecting an Auger electron or releasing an x-ray depends on the atomic number of the targeted atom; Auger electron emission is more probable in low Z elements, while x-ray fluorescence occurs more often in higher Z elements. For Sr, the fluorescence yield is 70% (Berger *et al.,* 2005). X-ray fluorescence originates predominately from the K shell emitting a set of characteristic x-rays depending on the mode of de-excitation. An electron de-excited from the L shell (n=2) to the K shell (n=1) emits K_α x-rays, while an electron de-excited from the M shell (n=3) to the K shell emits K_β lines. The energy and the intensity of the emitted Sr K x-rays are tabulated in table 1.1.

Table 1.1: Intensity of the Sr K shell x-rays per 100 shell vacancy (Firestone, 2005)

Line	Energy (keV)	Relative intensity
$K_{\alpha 1}$	14.165	39.1 ± 1.4
$K_{\alpha 2}$	14.098	20.3 ± 0.7
$K_{\beta 1}$	15.836	5.63 ± 0.20
$K_{\beta 2}$	16.085	1.00 ± 0.04
$K_{\beta 3}$	15.825	2.91 ± 0.1

The photons used to excite the sample originate from an x-ray tube or from a ϒ emitting radioisotope. Similar to NAA, the number of characteristic x-rays emitted and collected by the detector can be converted to the element's concentration in the measured sample. The shortcomings of bone Sr IVXRF is common for all elements emitting low energy characteristic x-rays and can be summarized as follows. Characteristic x-rays at lower energies than 40 keV attenuate heavily in the sample limiting the sample thickness/size that can be analyzed (Sutcliffe *et al*., 1996). It follows that Ca characteristic x-rays having energies of 3.4 keV are too low to be detected by a semiconductor detector, and thus Sr/Ca ratio cannot be evaluated directly. However, this shortcoming has been resolved by calibrating the Sr IVXRF system using standards having [Sr] relative to [Ca] in the bone mimicking phantoms. The second disadvantage for applying bone Sr IVXRF is that the human body is mainly composed of low Z elements, and thus Compton scattering is more prominent than coherent scattering at these low energies. This is not desirable as Compton scattering is the main contribution to the broad background in an IVXRF spectrum (Knoll, 1989). A higher background results in a higher uncertainty in distinguishing characteristic peaks from the background itself.

The effective dose received from an IVXRF measurement is generally orders of magnitude lower than received from neutron activation, making it more acceptable than NAA. For example, the effective dose from a 30 minute Sr IVXRF finger measurement is 10 nSv. The lower absorbed dose received during an IVXRF measurement compared with a neutron activation measurement and the low sensitivity of DPA warranted the development of IVXRF systems for measuring bone Sr. The Sr IVXRF system developed by our group has proven to have sufficient sensitivity in measuring Sr in healthy individuals as well as in following Sr levels from subjects under Sr supplementation (Zamburlini *et al*., 2007; Moise, 2010).

1.4 Bone Sr *In Vivo* X-ray Fluorescence

The first IVXRF system was developed to measure natural iodine in the thyroid using Dy-159 as the ϒ emitting radionuclide (Sutcliffe *et al.,* 1996). Other common elements measured using IVXRF analysis is: Cd, Hg, Au, U, and Sr (Sutcliffe *et al*., 1996; O'Meara *et al.,* 1999; Pejović-Milić *et al*., 2004)

Perhaps the most used and developed IVXRF system is the bone lead IVXRF system. Measurements of bone Pb have been reported as early as 1976 (Ahlgren *et al*., 1976). It has been adopted and further developed by Somervaille *et al.* (1985), Chettle *et al*. (1989), and Gherase *et al.* (2009) to name a few. A detailed description of the analysis of the bone lead system is presented elsewhere (Todd and Chettle, 1994).

There are several reasons why the development of bone lead systems forwarded at a faster pace than most IVXRF systems; Cd-109 emitting ϒ photons of energy 88.035 keV, just above the absorption K edge of Pb (88.005 keV), makes this couple advantageous over other systems, as it overcomes many of the common physical limitations of quantitative IVXRF. Because the incident photon and the fluorescent photons have similar energies, both the incident ϒ photons and fluorescent x-rays exhibit similar penetration depths, and thus correction for signal attenuation in soft tissue is not required. Furthermore, the fluorescent x-ray peak is only excited by the coherent peak, as Compton photons would have energies lower than the K edge for Pb. In fact, corrections for difference in sample content, sample size, and changes in experimental conditions, which are required with the IVXRF measurement, can be implemented in one step referred to as coherent normalization, which in turn refers to normalizing the characteristic photopeak area with the coherent photopeak area (Somervaille *et al.,* 1985). The efficacy of coherent normalization as a correction method differs from one XRF system to another, depending on several factors, which shall be discussed further in section 4.1.

As for Sr, four bone Sr IVXRF systems have been reported to date. Snyder and Secord (1982) modeled Sr retention in the skull of seven rabbits after the administration of Sr intravenously. Using Cd-109 as the excitation source and a 80mm^2 X 5mm^2 Kevex Si(Li) detector as the detection system, they obtained the biological half-lives for radioactive strontium. They were not however, interested in obtaining absolute Sr concentrations. In 1983, Wielopolski and colleagues were the first to perform IVXRF analysis on cadaver human legs with either Cd-109 or I-125 in 90° geometry (see figure 2.1 for an

example of a 90° geometry setup) (Wielopolski *et al.*, 1983). The authors obtained a minimum detection limit of 15 µg Sr/g wet bone. Yet, they were unable to quantify Sr in bone due to soft tissue attenuation.

Pejović- Milić and colleagues (2004) used a Cd-109 source to excite Sr at two measurement sites: the tibia and the phalanx representing trabecular and cortical bone respectively, at 90°geometry. With this set up, a minimum detection limit (MDL) of 110 µg strontium/ g Ca (corresponding to about 23 µg strontium/g cortical bone) was obtained.

Prior to *in vivo* measurements, the IVXRF system is calibrated by performing XRF measurements with external standards of known added concentration of the element of interest, which is Sr for this work. The fitted Sr areas are then plotted against the added [Sr] to create a calibration line. The MDL typically used in IVXRF analysis is defined as the minimum elemental concentration that produces a signal two times the uncertainty in a blank phantom's photopeak area, σ_0, divided by the slope of the calibration line:

$$MDL = \frac{2 \times \sigma_0}{slope} \qquad (2)$$

For *in vivo* measurements, Pejović- Milić and colleagues (2004) applied ultrasound to measure soft tissue thickness and correct for the attenuation of Sr x-rays in soft tissue using an analytical model, where the authors were then able to measure bone Sr levels in 20 healthy subjects. Unfortunately, measurements showed that the Sr levels from healthy subjects produced signals that were in the same order of the system's detection limit. Zamburlini and colleagues (2007) further developed the Sr IVXRF system initiated by Pejović- Milić (2001). Once the Cd-109 source was replaced by I-125 brachytherapy seeds and the subjects were positioned in 180° geometry (see figure 1.2 for an example of a 180° setup), the MDL of 22.9 µg Sr/g Ca after coherent normalization and 21.8 µg Sr/g Ca without normalization were reported.

The following sections summarize the improvements and steps taken for optimizing the source-based system originating from the work of Pejović- Milić (2001). An IVXRF system typically consists of an excitation source, calibration phantoms, and a photon radiation detector and associated ectronics used for pulse processing and data acquisition (Knoll, 1989). The choice of each component to best excite and

detect bone Sr was the first step of the development and optimization process. The second part included selecting the optimal geometry, subject to detector distance, subject to source distance, and finally optimizing the fitting function to best convert the Sr x-ray intensities to [Sr].

1.4.1 Selection of the Excitation Source for Bone Sr IVXRF

Selecting an excitation source with energies slightly higher than the K-edge of the element of interest is critical for any IVXRF measurement in the low energy range. That is because the Compton photons may overlap with the characteristic x-ray peaks increasing the background and lowering the signal to noise ratio. The K edge for Sr is 16.2 KeV and so the excitation source should be selected to emit radiation above this energy.

Among the available ϒ emitting radionuclides, Cd-109 and I-125 were found suitable for Sr excitation. Cd-109 decays to Ag-109 via electron capture or internal conversion and emits Ag K x-rays at energies 22.16 keV and 25.01 keV along with the 88 keV ϒ photons, while I-125 decays via electron capture and emits ϒ photons at energies 35.5 keV and Te x-rays. I- 125 is available in the form of brachytherapy seeds, Prostaseed® 125I. Therefore, I-125 brachytherapy seeds were selected as the excitation source for bone Sr IVXRF (Zamburlini, 2008). The I-125 brachytherapy seeds are absorbed onto five silver spheres and encapsulated by titanium. Each capsule is 4.5mm long and 0.8 mm wide. This source, aside from the photons emitted as a consequence of the I-125 decay, also emits Ag x-rays originating from the interaction of the source ϒ photons and x-rays with the silver spheres. The Ag x-rays increase the probability of Sr fluorescence compared to the I-125 radioisotope, as the photo-electric cross section for Sr at the 22.16 keV Ag x-rays is 48.3 cm^2/g, while the photo-electric cross section for Sr at 35.5 keV is 13.1 cm^2/g. As for comparing the performance of the Sr bone IVXRF system with the Cd-109 and the I-125 brachytherapy seeds, Zamburlini (2008) obtained lower detection limits and higher signal to noise ratios when the latter source was used after correcting for differences in dead time and source activity.

1.4.2 Measurement Sites and Bone Mimicking Phantoms for the Calibration of the Source Based Sr IVXRF System

The two measurement sites readily accessible for Sr IVXRF are the middle phalanx of the finger bone and the ankle bone. These two sites were chosen first, to have minimal overlying soft tissue, and secondly, to measure bone Sr at two sites having different proportions of cortical and trabecular bone (Pejović- Milić *et al*., 2002). The finger bone, or the middle phalanx, is mainly cortical (~ 60%), which is the harder layer of bone, while the ankle bone, the medial malleolus of tibia, is mainly trabecular (~ 55-75%), the softer portion of bone (ICRP 1995). Monitoring Sr levels at both sites simultaneously is essential, as it has been observed that Sr uptake in trabecular bone is faster than its uptake in cortical bone (Nielson, 2004).

The bone mimicking phantoms used to calibrate IVXRF systems are typically made of plaster of Paris (poP). PoP is produced from a soft mineral called gypsum, which is composed of calcium sulfate dehydrate ($CaSO4{\cdot}2H2O$) (Todd, 2000). The Sr doped finger phantoms were built cylindrically with a diameter of 7.5 mm and with a length of 60 mm, while the Sr doped ankle phantoms were shaped as a disk with a diameter of 27 mm and with a thickness of 10 mm. Unfortunately, Sr is inherently present in commercial poP at levels higher than levels observed from healthy individuals (Pejović- Milić, 2001). Therefore, in an attempt to produce poP bone phantoms with negligible Sr contamination, Zamburlini (2008) created Sr doped poP bone phantoms in house by starting with gypsum and then converting it to poP. The level of Sr contamination dropped from 600 to 50 ppm. Nevertheless, the improved poP still results in a calibration line with a non-zero intercept despite the lower Sr contamination level (figure 1.1). The Sr contamination is problematic, as Sr x-ray intensities corresponding to [Sr] lower than the contaminated Sr level will result in negative [Sr]. This limitation is discussed further in section 5.2.

1.4.3 Selection of the Detection System for the Source Based bone Sr IVXRF

Solid state detectors suitable for x-ray spectrometry in the low energy range (up to 50 keV) are usually silicon based such as the widely used Silicon Lithium Drift detector, Si(Li), and the recently emerging Silicon Drift Detector, the SDD. On the other hand, germanium based semiconductor detectors like the High Purity Germanium detectors, are preferred for higher x-ray/gamma ray spectrometry (Knoll,

1989). Throughout the development of the source based system, four different detectors available in house, two Si(Li) detectors, with different diameters, and two HPGe detectors, were tested. The main characteristics for each detector are provided in table 1.2.

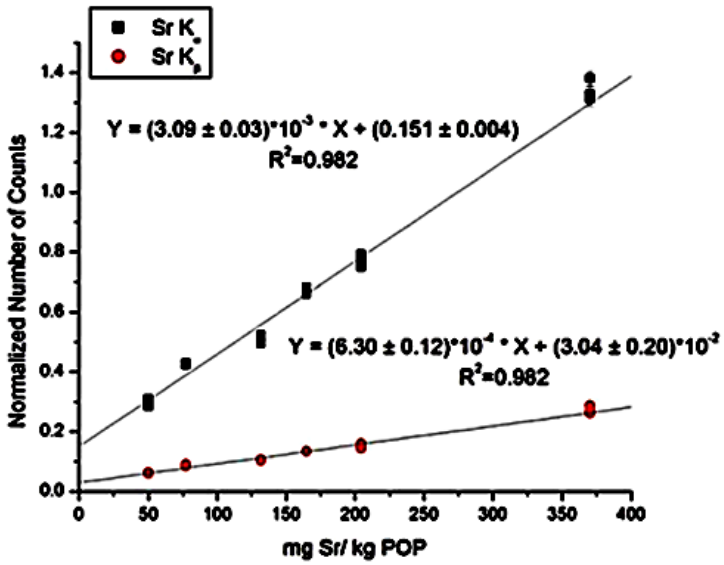

Figure 1.1: Calibration lines pertaining to Sr K_α and Sr K_β peak areas obtained following XRF measurements of Sr doped poP finger bone phantoms. The data were acquired using the Si(Li)-16 detector and I-125 brachytherapy seeds. The strontium K_α and K_β peaks were normalized to the 35.5 keV coherent peak (Zamburlini, 2008).

Table 1.2: Comparison of the main features of the solid state detectors available in house and that were compared for bone Sr IVXRF measurements (Zamburlini, 2008).

Detector Property	Si(Li)-10	Si(Li)-16	HPGe	HPGe-cloverleaf
Active diameter (mm)	10	16	50.5	4 X 16
Sensitive thickness (mm)	5.65	5.65	20	10
Be window thickness (mm)	0.5	0.05	0.5	0.5
Attenuation through Be window at 14.16 keV (%)	3	0.3	3	72
Energy resolution at 5.9 kev	175	209	369	509

Silicon based detectors provided a much simpler spectrum and a higher signal to noise ratio compared to the Ge based detectors (Zamburlini, 2008), which translates to a lower MDL. The simpler spectrum and higher S/N ratios from the Si(Li) detectors were due to the presence of the Ge x-ray escape

peaks. These peaks originate from the Compton photons at 25 keV located between the Sr $K_\alpha$and K_β,peaks, which deposit its energy 10.98 keV and 9.86 keV below the Compton energy peak. The Si(Li)-16 detector was chosen due to is higher geometrical efficiency than the Si(Li)-10 detector, proving to be a more essential factor than the latter's superior energy resolution.

1.4.4 Performance Comparison between Two Experimental Geometries: 90° and 180°

Two typical geometries adopted for IVXRF analysis are the 90° and 180° geometry. An IVXRF experimental setup is considered to be in 90° when the detector is placed in 90° with respect to the line formed by the incident photons and sample. The same definition is applied to 180° geometry or otherwise referred to as backscatter geometry. Although 90° geometry creates a lower background due to a smaller Compton continuum, 180° geometry is favorable especially for bone Sr IVXRF measurements for the following reasons (Zamburlini *et al*., 2006):

1) Subject positioning is much easier and is possible to reliably reproduce a measurement;

2) Sr fluorescent x-rays need to travel a shorter distance through soft tissue and are thus attenuated to a lesser degree;

3) Soft tissue correction is less challenging, because the incident photons travel the same distance to reach bone as the distance the Sr x-rays travel to reach the detector. Therefore, the source-based bone Sr IVXRF system is designed in the backscatter geometry.

1.4.5 Optimization of the Fitting Function

Following a sample measurement and the collection of an x-ray spectrum, the number of counts under the characteristic x-ray peak is fitted to determine the area corresponding to the x-ray intensity that is then converted to elemental concentration. Choosing the optimal mathematical function that best describes the photopeak is essential in any quantitative XRF analysis. Typically, in the case of *in vivo* trace elements, fitting is performed using a non-linear Levenberg-Marquartdt based routine (Bevington, 1969). The Sr characteristic peaks are fitted as Gaussian functions, where Sr $K_{\alpha1}$ and $K_{\alpha2}$ are fitted as one peak due to the small energy difference (67.1 eV) separating them, which is unresolvable with most solid

state detectors including the Si(Li)-16 used. Sr $K_{\beta 1}$ and $K_{\beta 3}$ are fitted as one peak as well for the same reason. Sr $K_{\beta 2}$ is separated from $K_{\beta 3}$ by 250 eV and is thus fitted as a separate peak. The background under the Sr peaks was fitted as an exponential function (Pejović -Milić *et al.,* 2004).

1.5.6 Further Development of the Bone Sr IVXRF

Following the selection of the parameters mentioned above, the source-based bone Sr IVXRF system was assembled and tested on humans. The system is comprised of I-125 brachytherapy seeds housed in a tungsten box and mounted on the Ortec EG&G Si(Li)-16 detector (figure 1.2). The Si(Li) detector is connected to the ORTEC DSPEC Plus™ multichannel analyzer operating Maestro™ software for count sorting and data acquisition. Both Heirwegh (2008) and Zamburlini and colleagues (2007) performed IVXRF measurements on healthy and osteoporotic patients taking Sr-based supplements. The system had shown enough sensitivity to measure reliably bone Sr IVXRF from both categories. Moreover, Moise (2010) demonstrated that the current source based bone Sr XRF system is also capable of showing changes in one's Sr level over time after the administration of low levels of Sr citrate. Yet, similar to the difficulties Snyder and colleagues (1982) and Weilopolski and colleagues (1983) encountered, an *in vivo* quantitative XRF measurement is not straightforward. The two main limiting factors are photon attenuation in soft tissue and the variability in the experimental conditions.

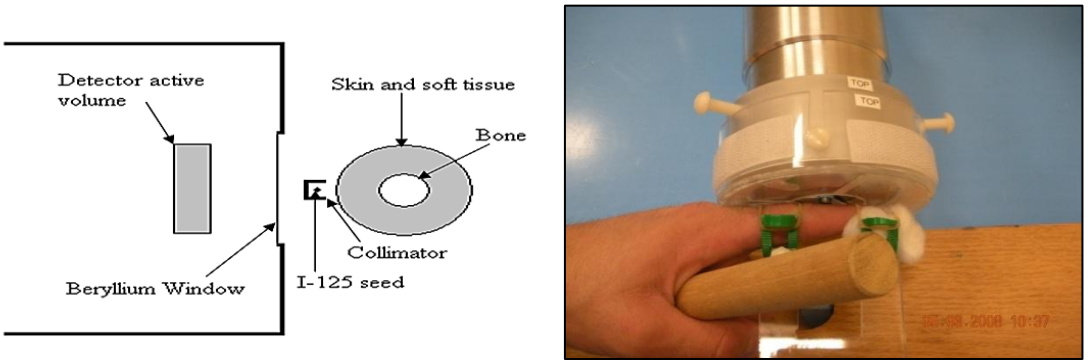

Figure 1.2:a) Schematic diagram of the source based system depicting the 180° geometry of the I-125 brachytherapy seeds and the Si(Li) detector with respect to the bone, b) Image of the source-based IVXRF setup with the finger positioned in 180°geometry with respect to the source and the detector (Zamburlini *et al.,* 2006).

The high success in quantifying bone lead by IVXRF, along with the increasing need to measure Sr in bone non-invasively, prompted Pejović- Milić (2001) and then Zamburlini (2008) to build and optimize the bone Sr IVXRF system. The atomic number, Z, of Pb is 82, while Z is 38 for Sr indicating that each element is governed by different photon-matter interaction cross sections. In the bone Pb IVXRF system, the Cd-109 excitation source photons are only 30 eV higher than the K absorption edge of Pb, and thus, both exhibit the same attenuation in soft tissue and in bone. Sr x-rays and photons from the I-125 brachytherapy seeds (I-125 ϒ photons and the Ag x-rays) however, have rather different energies and hence, exhibit different attenuation. The linear attenuation coefficients and the corresponding free mean path of Sr K_α, I-125 ϒ photons, and Ag K_α x-rays in cortical bone and soft tissue are tabulated in table 1.3. The mean free path length is defined as the average distance a photon travels before it interacts with an electron in the absorbing material.

It follows that by applying Beer-Lambert's law, 99% of the Sr K_α signal originates from a maximum depth of 2.26 mm in bone mineral and 99% of the Sr K_β signal comes from a maximal depth of 3.10 mm, and thus only the superficial layers of bone are sampled for Sr fluorescence.

Table1.3: The linear attenuation coefficient and the mean free path of photons emitted by I-125 brachytherapy seeds and the Sr fluorescent x-rays in cortical bone and soft tissue (Berger *et al.*, 2005).

Energy (keV)	Medium	Linear attenuation coefficient (cm^{-1})	Mean free path (cm)
Sr Kα 14.14	Cortical bone	19.8	0.051
Ag Kα 22.16	Cortical bone	5.46	0.18
I-125 ϒ 35.49	Cortical bone	1.61	0.61
Sr Kα 14.14	Soft tissue	2.15	0.47
Ag Kα 22.16	Soft tissue	0.71	1.40
I-125 ϒ 35.49	Soft tissue	0.33	3.00

Somervaille and colleagues (1985) were the first to apply coherent normalization to the K shell Pb peak. They found that the x-ray photopeak area divided by the coherent photopeak area correlated to bone Pb concentration, but more importantly, this ratio was found to be independent of changes in positioning, source activity, and geometrical factors such as the source to sample distance, sample size and shape. The authors also found this ratio corrects for photon attenuation from overlying soft tissue of

variable thickness. In principle, coherent normalization can be applied if the following conditions are satisfied (Somervaille *et al.,* 1985): (i) the incident photons are the only photons exciting the target element; (ii) the coherently scattered photons and the fluorescent photons have the same attenuation; (iii) Both the primary source photons and the characteristic x-rays should arise from the same region in the sample; (iv) The primary source and the characteristic x-rays should have the same coherent cross section distribution about the scattering angle. Criterion (i) is satisfied with the Cd-109 and Pb K x-ray couple as the coherent Cd-109 ϒ photons have energies just above the K edge of Pb. Criteria (ii) and (iii) are also satisfied, because both the incident ϒ photons and the characteristic Pb x-rays have almost the same energy, and thus have similar attenuation properties. Moreover following the same reasoning, Pb retains in bone, and thus the coherent photons activating Pb atoms ought to arise from bone as well. The last condition is satisfied as well for all scattering angles larger than 140°.

The coherent normalization could be applied to the bone Sr IVXRF as well if all four criteria are satisfied. For the Sr x-rays and I-125 ϒ photons couple, conditions (i) through (iii) are not satisfied. The coherent ϒ photons at 35.5 keV have energies 19 keV higher than the Sr K edge and therefore, Sr x-rays are not only excited by the primary source, but also by the Compton photons. As shown in table 1.3, at these low energies, the linear attenuation coefficient in soft tissue increases sharply with decreasing E, and so the attenuation at the Sr x-ray energies (14.14-16.02 keV) is much higher (six times higher) than the attenuation at the coherent ϒ photon energy (35.5 keV). Thus condition (ii) is not fulfilled as well. Sr is a bone seeking element; hence, Sr signal originates from bone only, however it has been reported that 30% of the coherent ϒ photons arise from soft tissue (Zamburlini *et al*., 2008). In backscatter geometry, Sr fluoresced by the coherent ϒ photons, do in fact have more or less similar angular distribution at scattering angles 140°-180°. Although the last condition is the sole condition satisfied in the source-based bone Sr IVXRF system, coherent normalization has been proven to reduce the Sr signal's dependency on geometrical factors and source activity (Zamburlini *et al.,* 2008; Heirwegh, 2009). It does not however, correct for signal attenuation in soft tissue overlying the finger and ankle bone.

Weilopolski and colleagues (1983) were the first to propose the use of an ultrasound system for the attempt to correct for Sr signal attenuation through soft tissue. Pejović- Milić and colleagues (2002) had also found that ultrasound imaging was necessary to determine the thickness of soft tissue and correct for Sr attenuation. In fact, 2 mm of soft tissue attenuates the Sr x-rays by 35%, while 4 mm of soft tissue attenuates the Sr signal by 58% (Berger *et al.*, 2005). This is put into context considering the average soft tissue thickness overlying the finger bone in humans is estimated to be 2.9$\pm$ 0.6 mm

(Pejović- Milić *et al.,* 2002). The ultrasound system is operated at a maximum frequency of 10 MHz and a central frequency of 8MHz with a spatial resolution of 0.2 mm. The level of accuracy using this ultrasound system, determined as the deviation of the soft tissue thickness obtained following an ultrasound measurement from the average thickness estimated from other imaging modalities of the same sample (MRI, CT, and high frequency ultrasound system), was evaluated by Heirwegh and colleagues (2010) to be 6.6%. It was later demonstrated that the reproducibility of repeated ultrasound measurements was improved by the presence of a gel pad mediated between the transducer and the subject's skin (Moise, 2010). However, the finger measurement was found to have a lower precision (12%) than an ankle measurement (3.4 %), possibly due to the latter's planar geometry (Moise, 2010).

An additional correction applied to quantitative IVXRF is required to account for differences in matrix composition between the calibration phantoms and the sample being analyzed. In the case of bone Sr IVXRF, as well as bone Pb IVXRF analysis, difference in matrix composition of bone and poP is accounted for by correcting the characteristic x-ray intensity of the element of interest using the coherent conversion factor (CCF), defined by Todd (2000) as the ratio of coherent cross section of human bone to that of poP. An example of how this correction is applied is provided in the work of Heirwegh (2008).

The paradoxical dual effect of strontium has prompted researchers to further study the kinetics of Sr in human bone, especially if taken as an anti-osteoporotic drug. Questions such as how much strontium is safe for it to remain beneficial or how long should patients be supplemented for are just a couple concerns that need to be addressed immediately. Since 2008, our group has been recruiting healthy, osteopenic and osteoporotic individuals, who are self-supplementing Sr citrate instead of Sr ranelate. That is because the latter is not yet approved by the Ministry of Health in Canada nor is it FDA approved in the United States. Sr carbonate, Sr lactate, Sr chloride, and Sr ranelate have all been proven to have the therapeutic effect on the calcification of bones; however whether one is better than the other is yet to be determined (Marie *et al.,* 2001; McCalsin *et al*., 1959; Grynpas *et al.,* 1999; Meunier *et al*., 2009). The interested reader is encouraged to read the work of Moise (2010) for more on Sr uptake and retention in human bones following low dose of Sr citrate.

Despite the major improvements in the overall sensitivity and reproducibility of Sr IVXRF measurements after the two step correction (soft tissue attenuation of Sr signal and coherent normalization), the source-based system can only monitor relative changes in Sr levels over a course of time, partly due to the incomplete soft tissue correction currently applied, and partly due to the physical

limitations of the polychromatic excitation source and the detection system. The intensity of the excitation source is not constant as well, and because I-125 has a half-life of 59.4 days, it needs to be replaced regularly. Its modest intensity requires *in vivo* measurements to be 30 minutes long in order to obtain reasonably high S/N ratios. Furthermore, optimal energy selection of the source is limited as I-125 emits multiple x-rays, such as the simultaneous emission of Ag and Te x-rays, along with the coherent Υ rays. This can be translated into a complex spectrum with a high background under the Sr characteristic x-ray peaks, thus worsening the sensitivity of the system to detect Sr. In fact, in the case of IVXRF measurements, the subject receives a radiation dose that may not necessarily lead to Sr excitation. In addition to the high background produced from Compton scattering, the Si(Li) detector used has a limited resolution of only 289 eV at the Sr K_α x-ray energy, where it fails to resolve Sr x-ray fluorescent peaks completely separate from the Ag Compton peaks.

As mentioned earlier, Sr in bone influences the BMD and bone mineral content measured by DEXA, owing to the fact that Sr has a higher atomic number than Ca, and thus attenuates x-rays to a higher degree (Nielson *et al*., 1999). Since DEXA is the most widely used diagnostic tool for osteoporosis recommended by WHO, patients on Sr therapy will have false over-estimated BMD values. Nielson and colleagues (1999) have addressed this issue and developed the following formula to correct for the false BMD values:

$$BMD\ (adj) = BMD(n)/[\ 1 + C.SrL(n)] \qquad (3)$$

where BMD (n) is the experimentally determined value for a sample of bone with Sr level SrL(n) and C is the correction factor (~ 0.1). This suggested correction is important, because the over-estimated BMD values in the case of Sr based treatment for osteoporosis can only be adjusted if the [Sr] in bone is known.

Therefore, the need to distinguish between healthy Sr doses and toxic levels, as well as to determine [Sr] in the bone with a high level of certainty to correct for the over-estimated BMD values measured by DEXA, warranted the development of a diagnostic tool for measuring bone Sr *in vivo.* Due to the limitations of the source-based bone Sr IVXRF system, the second generation of this diagnostic tool has been developed.

The objective of the work presented here is developing a new bone Sr IVXRF system, which will overcome the physical limitations of the source-based system by providing a lower detection limit with a higher level of accuracy and precision.

The optically focused IVXRF system consists of a Ag target x-ray tube coupled with a doubly curved optics (DCC) used as the monochromator. The system's detection system consists of a silicon drift detector (SDD) with its pulse processing unit connected to a computer. The following chapter provides a detailed description of the newly built optically focused IVXRF system, while characterizing each component, the x-ray tube and the detector. The chapter also includes testing three different detectors available in house. Chapter three describes the intermediate steps taken to select the optimal parameters to run the optically focused IVXRF such as sample to detector distance, sample to source distance, and the geometry of the experimental setup. Subsequently, chapter four investigates different signal normalization techniques that best corrects for experimental and geometrical factors. In this chapter, a different approach for the evaluation of soft tissue is also proposed. Finally to cap off this manuscript, a list of recommended analysis and work to further optimize the second generation of bone Sr IVXRF is provided in chapter five.

Chapter 2 Preliminary Steps towards Optimizing the Optically Focused IVXRF System

The previous chapter highlights the steps taken to develop and optimize the source-based Sr IVXRF system. This chapter introduces the second generation of bone Sr IVXRF, the optically focused IVXRF system. In addition, it characterizes the two basic components of the system: the x-ray tube and the solid state detector.

2.1 The Optical System

The optically focused IVXRF system is a custom built system and consists of a silver target x-ray tube coupled with a doubly curved crystal (DCC) as the excitation source. The optical systems is referred to the silver target x-ray tube coupled with the DCC, while the silicon drift detector along with its digital processing electronics, forms the detection system. The latter addition is necessary to abide the high incoming flux with acceptable dead time.

Prior to purchasing the optical system, Zamburlini *et al.* (2008) performed preliminary measurements with the Ag and Mo target x-ray tube coupled with the DCC optics at the X-ray Optical System (XOS) company in Albany, USA. XOS is one of the first groups to manufacture doubly curved crystals after developing the novel crystal-bending technology (Chen *et al.*, 2008). The signal to noise ratios (S/N) from both the Mo and the Ag target x-ray tube were used as a means to compare and select the most suitable x-ray target for Sr fluorescence. The S/N is defined here as the area under the Sr K_α peak divided by the square root of the area of the background under that same peak. The Vortex Silicon Drift Detector (SDD) with an active area of 50 mm^2 and a crystal thickness of 0.35 mm available at that time at XOS was positioned at either 160° or 135° geometry with respect to the phantom (tibia and finger phantom) and the x-ray tube. It was concluded that because Mo has a Compton peak at 16.2 keV, the Sr K_β peak was unresolvable from the Mo Compton peak, thus resulting in a lower S/N ratio than that obtained from the Ag target. Furthermore, the 22.16 keV Ag K_α x-ray energy was shown using Monte

Carlo simulations -code EGS4- to be the ideal incident energy for Sr excitation. Subsequently, Zamburlini (2008) suggested the design of a shielding box necessary to comply with licensing requirements for x-ray shielding defined by the Ministry of Labor of Ontario. The shielding box was built from Plexiglas with dimensions 120 cm X 135 cm X 80 cm and with a thickness of 0.635 cm to attenuate the x-ray beam to the regulatory limit of 25µSv/hr. In addition, a Cadmium beam stopper is placed at the end of the box in the direction of the beam. As another safety procedure, the side window is interlocked with the x-ray power supply and a light tower is mounted on top of the box to indicate when the tube is in use (figure 2.1)

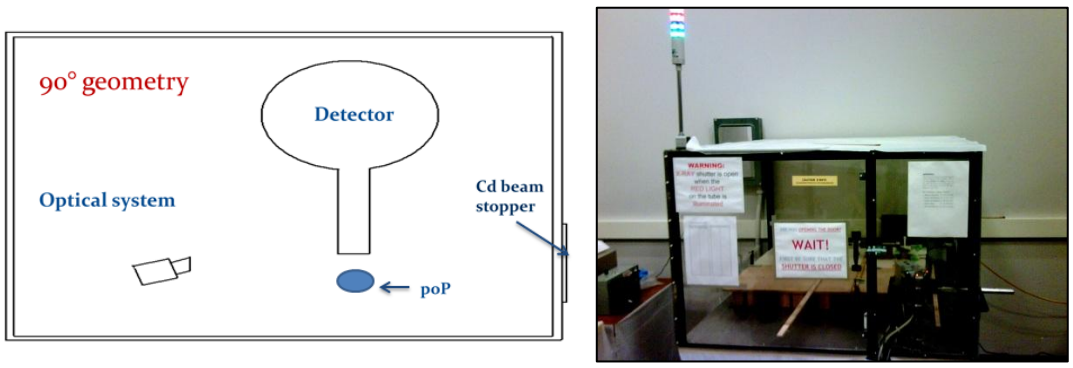

Figure 2.1: a) Schematic diagram of the optically focused IVXRF system in the shielding box depicting the position of the optical system, Sr doped poP phantom, and detector positioned in 90° geometry with respect to the poP and optical system, b) Image of the shielding box depicting the Cd beam stopper, the light tower and the power supply.

XOS provides several optical systems for high definition x-ray micro XRF analysis, such as polycapillary optics, and for high definition monochromatic micro XRF analysis, such as doubly curved optics coupled to an x-ray tube. Both optical systems can be used for the analysis of small features and trace element analysis with enhanced spatial resolution, hence improving the overall sensitivity of the XRF measurement. The polycapillary optics focuses the divergent x-ray beam directed to a small sample spot of a few microns, while the doubly curved crystal (DCC) selects the energy emerging from the tube and focuses it to a micron-sized x-ray beam directed on a small sample area (www.xos.com). The latter has made portable, in situ, remote, larger working distance and simpler quantitative measurements possible (Chen *et al*., 2008). DCC optics is based on the Bragg's diffraction law:

$$n\lambda=2d\sin\Theta \qquad (1)$$

where λ is the wavelength of the diffracted beam, n is the integer indicating the order of diffraction from crystal planes of spacing d, and Θ is the angle between the incident beam and the Braggs planes.

In 1993, Johansson showed that bending the monochromator crystal at a uniform curvature yields a major increase in the beam intensity as the Bragg condition is satisfied over a large range of angles in the divergent incident beam (Chen *et al*., 2008). Curving the crystal plate also focuses the output beam producing a narrow band-pass and thus improving the energy resolution of the divergent beam. For maximum reflection off the crystal, a well-defined geometry, known as the Roland circle is used: the incoming beam, the monochromator and the exiting diffracted beam should all lie on the same circle as shown in figure 2.2.

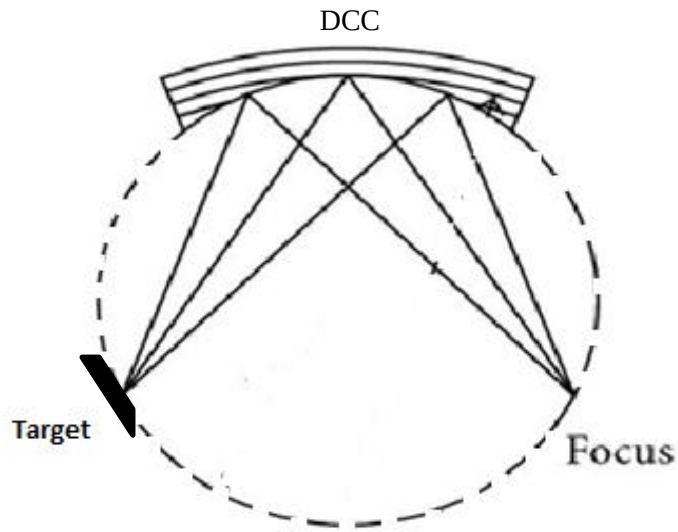

Figure 2.2: Side view of the focal circle with illustrative x-ray beams emitted at the left and reflected to the right side as well as the lattice planes in the bended crystal (Chen *et al*., 2008).

The crystal monochromator can vary from application to application, where the most common crystals used are germanium, diamond, graphite, quartz and silicon. The silicon crystal is the type present in the optical system used in this work. Energy selection is possible by choosing the proper crystal and the proper grazing angle (Chen *et al*., 2008). The bending crystal is a toroid, where the bending radius of the crystal is perpendicular to the Roland circle. Such geometry renders point to point

focusing where the source spot is imaged at the point labeled focus in figure 2.2. The material of the target Ag, is chosen to select and focus the emerging x-ray beam of energy 22.16 keV to best excite Sr atoms with K absorption edge of 16.2 keV in the bone. Furthermore, DCC optics filters out bremsstrahlung radiation emitted from the tube so that characteristic x-rays of the target, in this case Ag x-rays are the only x-rays available for Sr excitation. Therefore changing the excitation source from a radio-isotope to an optically focused x-ray tube directed at the measured bone site is expected to improve the detection limit and the overall accuracy of measurements by lowering the overall background in the obtained spectrum, thus improving the system's sensitivity to measure Sr.

2.1.1 Beam Imaging and Primary Selection of the Sample to Source Distance According to Beam Size

For the case of IVXRF measurements, the beam size is preferred to cover the whole measured bone site, the middle phalanx. The size of the latter is approximately 1 cm^2 and thus a beam area just smaller than 1 cm^2 is ideal to reduce the scattering of the beam off overlying soft tissue. A fellow graduate student, Elstan Desouza, had previously imaged the beam at different distances and found the focal distance to be 30 cm away from the tube.

The x-ray beam was imaged with radio-chromic films of size 50 mm X 20 mm (Harpell Associates, Oakville), which are designed for dosimetry and calibration of medical linear accelerators. These films were placed in a plastic holder along the path of the beam for as long as it was required in order for a dark image to form. These films were re-aligned with the line of the beam if the resulting intensity profile was not centered more or less at the horizontal distance of 25 mm. They were also placed at different distances away from the optical system using a red laser mounted on top of the tube (Melles-Griot, Ottawa). The images obtained were then scanned and processed with ImageJ, the image processing system developed by NIH (www.imagej.nih.gov. com). The images produced rather low signal to noise ratios as these films are intended to image higher x-ray energies (100kV-MV) than the ones emitted by this x-ray tube. A sample gray scale image of the beam at the focal length is illustrated in figure 2.3. Figure 2.4 illustrates the beam's intensity profile as a function of horizontal distance along the surface of the film. Based on figure 2.4, one can conclude that the beam is nicely focused and centered (beam spot is located at a horizontal distance of 25 mm from one side of the film) for distances

shorter than or equal to the focal length, 30 cm. At farther distances, the beam disperses with its intensity being less focused compared to the beam's profile at shorter distances. One also observes from figure 2.3 and 2.4 that the beam has two horizontal "spots", which appears even at the focal distance, and thus, is not due to deterioration of the beam quality with distance.

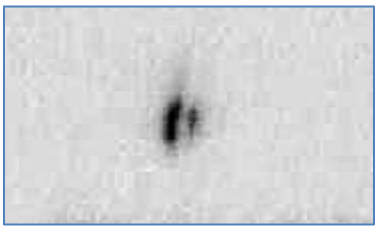

Figure 2.3: Gray scale image of the beam at the focal length imaged using radio-chromic films (Elstan Desouza, unpublished work).

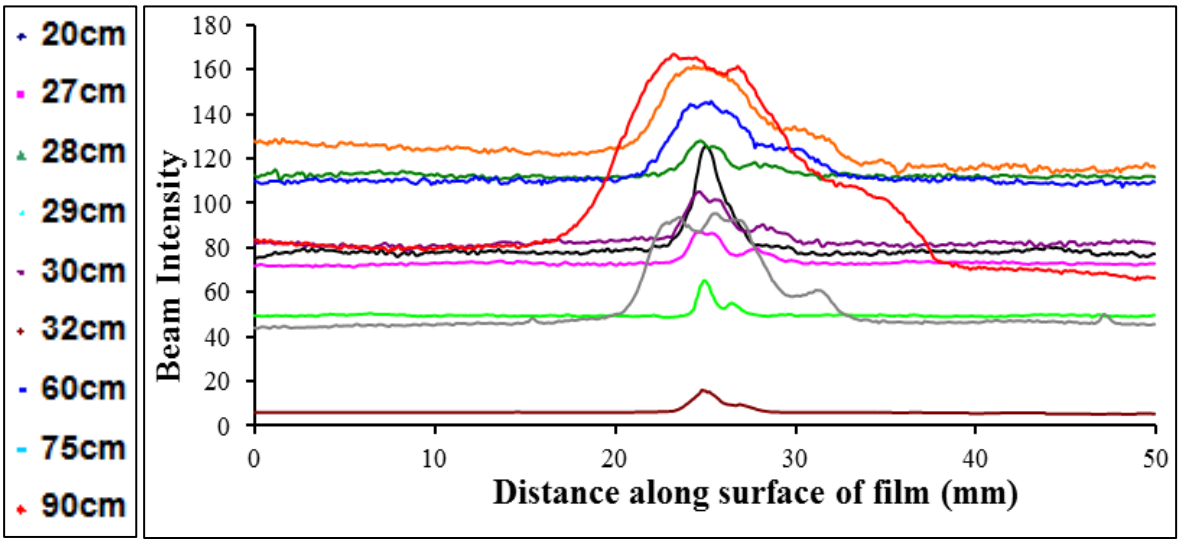

Figure 2.4: Graphs of the beam intensity with horizontal distance along the surface of the film. Each graph corresponds to a distance from the x-ray tube. The film is 50 mm wide (Elstan Desouza, unpublished work).

Finally, the beam area was determined after measuring the height and width of the beam spot from the obtained images. Table 2.1 demonstrates that for Sr IVXRF measurements, only two distances of coordinates (70, 7.2) cm and (78.1, 7.3) cm, where the first and second coordinates correspond to the horizontal distance from the x-ray tube and the height of the beam spot from the base of the shielding box respectively, resulted in beam areas that are comparable to the irradiated area of the measurement site, the middle phalanx of the index finger.

Table 2.1: Dimensions of the beam spot at different distances from the x-ray tube. Random distances were chosen (Elstan Desouza, unpublished work).

Distance (cm)	Width (mm)	Height (mm)	Area (cm^2)
30.0	2.21	1.57	0.023
43.9	4.74	2.09	0.09
50.0	6.75	3.56	0.19
62.8	10.13	7.01	0.64
70.1	11.50	8.79	0.96
78.1	11.70	11.00	1.09
101.5	19.41	16.33	2.88

Hence, the optical system is designed to produce a micro-focused monochromatic x-ray beam until the focal distance. Beyond 30 cm, the beam expands from an area of 0.023 cm^2 to a maximum area of 2.88 cm^2. Therefore, the sample to source distance may be selected to produce an x-ray beam relevant to one's application. For this work, two distances 70 and 78.1 cm are recommended as the primary choices for Sr IVXRF measurements.

2.2 Selection of the Detection System for the Optically Focused IVXRF

As mentioned in section 1.5, silicon based detectors are more sensitive to detect radiation in the lower energy range similar to our application. The Ortec EG&G Si(Li)-16 was chosen over the Ortec EG&G Si(Li)-10 due to its larger active area, which resulted in higher count rates. The Si(Li)-16 (referred to as the Si(Li) detector from this point on) is connected to the digital electronic processing unit, the DSPEC Plus ™ Digital Gamma Ray Spectrometer and the Maestro™ software (www.ortec-online.com). Pejović- Milić (2001) selected operating parameters such as flat top (0.8µs), cusp constant (0.8µs), rise and fall times (10µs) to optimize the system's detection for Sr IVXRF measurements. These parameters control the time for the detector to shape the pulse. Presently, SDDs are considered to be among the fastest high resolution detector system for x-ray spectroscopy. Being compact and portable, SDDs are being widely used in diffractometry, element imaging in scanning electron microscopes and synchrotron applications, in addition to art preservation analysis, archeometry and environmental analysis (Lechner

et al., 2001).The main advantage of the SDD detector is its small anode capacitance allowing a short rise time to shape the signal with yet a high resolution (Lechner *et al.,* 2004). The total readout capacitance is further minimized as the n-JFET amplifying transistor is integrated on the center of the detector chip. The small capacitance not only translates into extremely high count rates (~ 10^5 cps), but also makes the SDD rather insensitive to electronic noise, and thus resulting in very low leakage current of which is typically in the order of 100pA/cm^2. In fact, because of the advanced process technology, the SDD can be operated at room temperatures or with moderate cooling (Lechner *et al.,* 2004). It was shown that for a typical 10 mm^2 SDD operated at a temperature of -15°C, the energy resolution (FWHM) at the Mn K_α line (5.9 KeV) is 147 eV and the pulse shaping time is in the order of 100 ns (Lechner *et al*., 2004). Lechner and colleagues also varied the shaping time from 70 ns to 450 ns and showed that with an Fe-59 radioactive source and as a worst case scenario, a rising time of 70 ns at 10^6 cps still resulted in an energy resolution of 250 eV, which was found comparable to a Si(Li) detector having a rising time of 10µs (figure 2.5).

The VITUS R100 Silicon Drift detector, referred to in this work as the Zr-collimated SDD, was purchased from Ketek GmbH (Germany). The Zr- collimated SDD was first tested on the source based IVXRF system using the I-125 brachytherapy seeds as the excitation source and the highest concentration Sr-doped phantom labeled 2ppm (1375.04µg Sr/g Ca). The seeds were housed in the tungsten (W) box on the same plastic holder used for the Si(Li) detector (see figure 2.6). Because the Zr-collimated SDD's window has a diameter of 11.06 mm and an active diameter of 10.8 mm, this source holder is occluding the majority of the collected photon counts. At the time of the first XRF measurements with the Zr-collimated SDD, a source holder customized for the detector had not been built yet, and thus the same source holder used for the Si(Li) detector was used for the Zr-collimated SDD, rendering backscatter geometry (figure 2.6). The experimental setup is thus the same as the current source based IVXRF system (figure 1.2) with the Zr-collimated SDD replacing the Si(Li) detector.

Within seconds of the first measurement, the K_β Sr peak showed a higher peak intensity than the Sr K_α, suggesting the presence of another element (figure 2.7). Tables for x-ray fluorescence intensity indicated that Zr (Z=40 and A= 91.2) emits fluorescent x-rays at 15.78 keV and 17.7 keV (www.ie.lbl.gov/atomic/x2.pdf). Exposing the Zr collimated SDD to the Mo-97 and Ag-109 radioisotopes in front of the 2ppm Sr doped phantom still produced the Zr peaks, which thus confirmed that the Zr was not present in the source holder. Moreover, a Sr free resin -based hand phantom was measured

with the variable sources as well, which resulted in the same conclusion. Thus it was concluded that the Zr originated from the rim of the SDD as an external collimator.

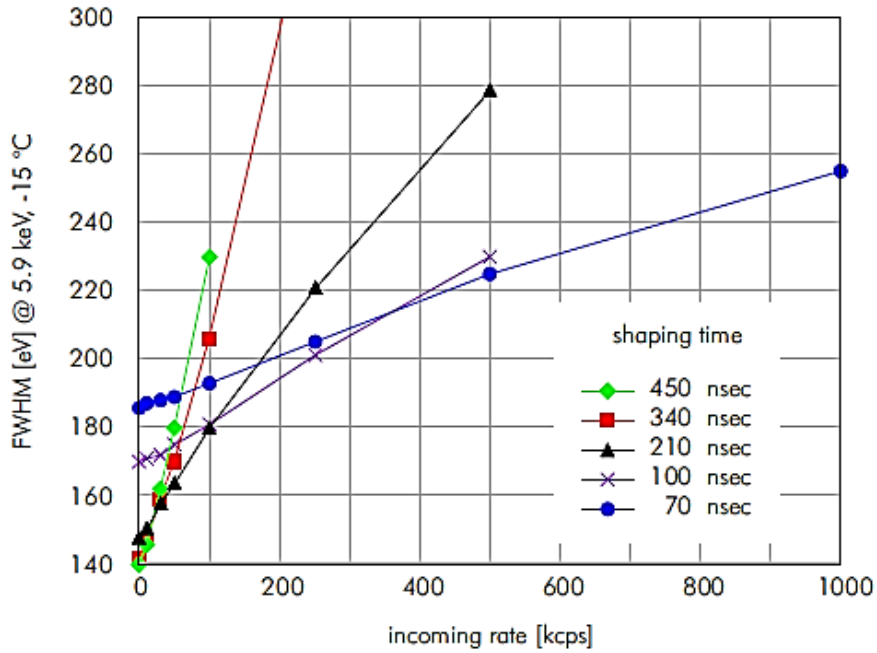

Figure 2.5: Measured count rate dependent energy resolution of an SDD with analog pulse processing system at a temperature of -15 °C. With the shortest shaping time of 70 nsec the system is still able to operate at 10^6 incoming photons per sec with a throughput of $4 \cdot 10^5$ processed counts/s (Lechner *et al.,* 2004).

.

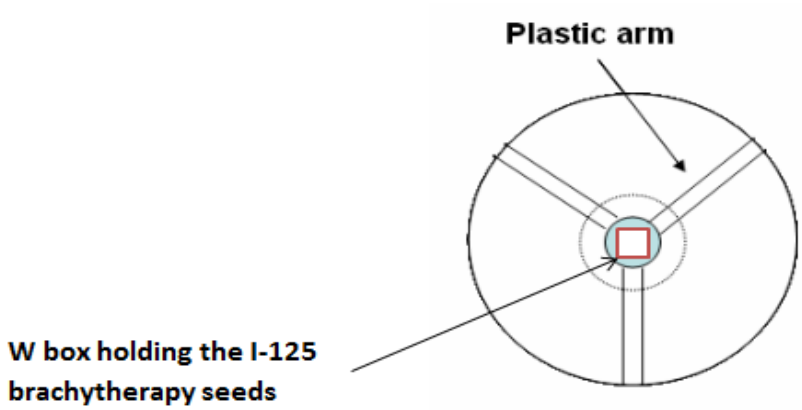

Figure 2.6: Front view of the source holder mounted on the detector window. The rectangle in the middle represents the collimator, which hosts the brachytherapy seeds. The dashed circle represents the detector's active area of the Si(Li) detector. The plastic arms are shown as well.

Consequently, W shielding was designed for sufficient signal collection by the detector and for sufficient shielding to prevent Zr activation. W was chosen and purchased with 5% nickel impurity (www.tungsten.com) so that first, it could easily be machined to our specific purpose. Secondly, since W is a high Z element (Z= 74), a thickness of 1 mm was sufficient to attenuate the Zr x-rays emerging from the edge of the detector. Figure 2.8 depicts a side view image of the detector's head with the W shielding.

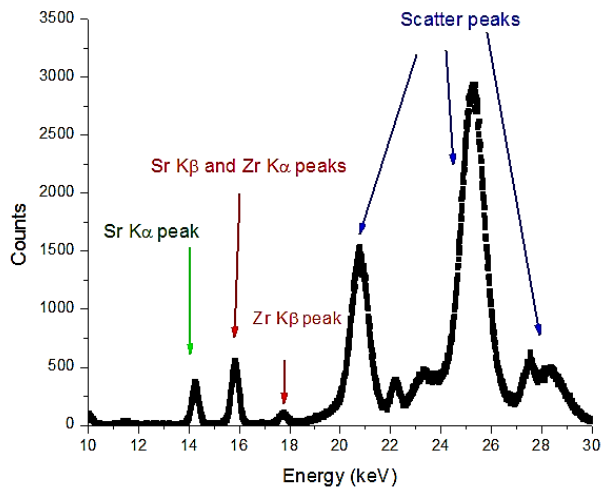

Figure 2.7: Bone Sr phantom spectrum collected by the Zr collimated SDD with the brachytherapy seeds as the excitation source. Zr x-ray peaks at 15.78 and 17.7 keV originate from the SDD; therefore Zr at 15.78 overlaps with Sr Kβ at 15.8 keV.

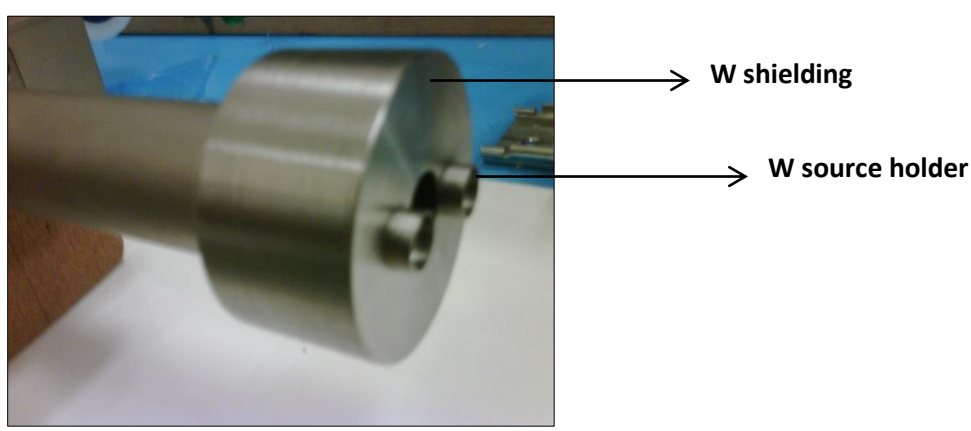

Figure 2.8: Side view image of the W shielding of the Zr collimated SDD with two source holders for the I-125 brachytherapy seeds.

A whole set of phantom measurements were then performed on the source-based system in backscatter geometry using the Zr-collimated SDD rather than the Si(Li) detector. The brachytherapy I-125 seeds were planted in circular W holders built on the W collimator (figure 2.8). A higher signal to noise ratio was observed when the seeds were planted on the same side of the collimator, i.e. in one circular holder. Unfortunately, Zr was still present in the spectrum, and thus shielding the edge was not sufficient to eliminate Zr contamination. It was concluded and confirmed by Ketek GmbH (Germany) that Zr was actually used as the internal collimator clipped on the Si wafer instead. Since the W shield was aimed to cover the Zr on the SDD's edge and not the Si wafer, the detector's active diameter was reduced to 10.8 mm. Subsequently, a means to reduce the active area was needed to eliminate Zr fluorescence. Different opening diameters of copper disks were made as an attempt to further shield Zr. The copper disks' thicknesses ranged from 0.8 mm to 2.4 mm, while the diameter of the opening ranged from 1 mm to 9 mm. The largest opening to eliminate Zr was found to be a combination of two 5 mm and two 9 mm disks, each of thickness 0.8 mm. Nevertheless, the counting statistics associated with both Sr x-ray peaks were low, preventing peak fitting, due to the use of the W and Cu collimator. Therefore, when the Zr-collimated SDD detector was used, only Sr k_α areas were used to extract the MDL as described in the following section. Another disadvantage of this detector was that the maximum energy output was set only to 30 keV, hence not collecting the I-125 coherent peak at 35.5 keV, and thus making coherent normalization unfeasible, which is important to correct for variations in several experimental factors (section 1.5).

2.2.1 Performance Comparison of the Si(Li) and the Zr-Collimated SDD Detector with I-125 Brachytherapy Seeds on the source-based Sr IVXRF System

The source-based IVXRF system, presently in clinical use, consists of the Prostaseed® I-125 brachytherapy seeds and its detection system. The latter is composed of the EG&G Ortec Si(Li) detector with its pulse processing unit, Ortec® DSPEC PLUS™ Digital Gamma Ray Spectrometer and Maestro™ software. A detailed description of the system was given in section 1.5, and the schematic diagram of the experimental setup is illustrated in figure 1.2a. I-125 brachytherapy seeds were inserted in the tungsten collimator with a 5mm internal diameter, 5.4 mm external diameter, and a length of 3mm. This collimator is centred on a plastic holder (see figure 2.6) and mounted on the Si(Li) detector. The Sr-doped poP resembling the shape of a finger bone was positioned horizontally in front of the detector 0.8

cm away rendering backscatter geometry. Each phantom was measured three times in random sequence for 1800 s real time. The dead time recorded was 18%. The data was acquired and processed using the ORTEC DSPEC Plus™ multichannel analyser operating Maestro™ software connected to a computer. For each measurement, the Sr $K_{\alpha 1}$ and $K_{\alpha 2}$ were treated as one peak, Sr K_{α}, and fitted as a Gaussian function with a linear background using the non-linear curve fitting tool in OriginLab Pro software. Sr K $_{\beta 1,3}$ peaks were not analyzed at this point due to the Zr interference with these peaks when the Zr collimated SDD was used as discussed above. Furthermore, because the Zr collimated SDD had a maximum output energy range of 30 keV, the 35.5 keV coherent peak was not registered on the detector, and thus coherent normalized MDL could not be performed when this detector was used. Hence, the coherent normalized MDL was not provided.

The Si(Li) detector was then replaced by the Zr collimated SDD to test its performance with the I-125 brachytherapy seeds. Table 2.2 shows a summary of the detectors' main properties. The same geometry and phantom to detector distance was used as during the previous setup. With the Zr-collimated SDD, the I-125 brachytherapy seeds were planted in the W source collimator located on one side of the W shielding (figure 2.8). Once again, a full set of phantom measurements were performed three times for a real time of 1800 s each. In this case, the dead time recorded was 1.5%. The data was acquired and processed using the digital pulse processing unit and the AXAS VITUS acquisition system connected to a computer. Spectra pertaining to Sr K_{α} peaks were fitted using OriginLab Pro as a Gaussian function with a linear background.

Table 2.2: Summary of the main properties of the three silicon detectors used throughout this work

Properties	Zr-collimated SDD	Si(Li)	Multi-element collimated SDD
Energy resolution at 5.9 keV (eV)	160 -162	220	139-141
Detector's active area after collimation (mm^2)	91.6	200	80
Sensitive thickness (mm)	0.450	5.65	0.450
P/B ratio	400	N/A	6065
Shaping time (µs)	3	10	3

The MDL was chosen as the parameter to compare the sensitivity of each source-based system: the Si(Li) detector with I-125 brachytherapy seeds and the Zr collimated SDD with I-125 brachytherapy seeds under the same experimental conditions (geometry and phantom to detector distance). Since, coherent normalization was not performed the direct Kα MDL were obtained from the Sr Kα peak areas corrected for the activity of the source, because the conducted experiments were extended over a couple of weeks. A calibration line was formed allowing for the calculation of the direct Kα MDL. A summary of the obtained direct Kα MDLs is summarized in table 2.3.

Table 2.3: Summary of the direct Kα MDLs obtained from the two source-based system: The Si(Li) detector with I-125 seeds and Zr collimated SDD with I-125 in backscatter geometry.

Experimental setup	Direct Kα MDL
Si(Li) +I-125 in 180°	$22.45 \pm 0.60 \frac{\mu g\ Sr}{g\ Ca}$
Zr collimated SDD + I-125 in 180°	$27.59 \pm 0.84 \frac{\mu g\ Sr}{g\ Ca}$

Although, the Zr-collimated SDD has superior energy resolution (table 2.2) and high throughput apparent in its low dead time, the source-based system using the Si(Li) detector produced a slightly lower MDL than when the Zr collimated SDD was used. The higher resolution of the Zr collimated SDD to that of the Si(Li) detector did not improve the S/N ratio or the MDL. The S/N ratio is defined here as the area of the Sr Kα peak divided by the error in that area. The S/N for the Zr-collimated SDD was found to be 95.7, while it was found to be 109.4 for the Si(Li) detector. The lower MDL observed is due to the larger solid angle (25 sr vs. 12 sr) allowing a larger number of photons to be counted and thus allowing having better counting statistics. The solid angle is defined in this work as the detector's active area divided by the square of the sample to detector distance. Moreover, for this experimental setup, only direct MDLs were compared, since the 35.5 keV ϒ photons were not observed on the Zr collimated SDD. Therefore these results are insufficient to conclude which detector is more suitable for Sr IVXRF on the optically focused IVXRF system.

To address the Zr contamination and energy cut-off at 30 keV, the group successfully negotiated with Ketek GmbH (Germany) to replace the Zr-collimated SDD detector with a multi-element collimated SDD that would eliminate interfering peaks near the Sr and the Ag energies (14 keV to 30 keV). In

addition, the energy range was extended to 40 keV so that coherent normalization would be possible with 35.5 coherent ϒ photon peaks when used with the source based Sr IVXRF system.

The most relevant properties of the multi-element collimated SDD is summarized in table 2.2. The FWHM of the Mn Kα x-ray at 5.9 keV and the peak to background ratio (P/B) was confirmed to be as stated by Ketek GmbH (table 2.2). The P/B ratio is defined by Ketek GmbH as the number of counts at the Mn Kα divided by the number of counts at the lowest peak in the Compton continuum. The multi-element collimated SDD does not only have multiple elements as the detector's collimator, but also each element is layered with a different thickness, as shown below in table 2.4. This collimator design prevents fluorescence of a single element present in the detector to interfere with characteristic x-ray peaks originating from the sample.

Table 2.4: Composition of the SDD's multi-element collimator

Element present in the detector's collimator	Layer thickness (mm)
Ta	0.15
Cr	0.032
Ti	0.015
Al	0.06

2.2.2 Performance Comparison of the Si(Li) and Multi-Element Collimated SDD Detector on the Optically Focused IVXRF

A detailed description of the optical system was provided in section 2.1, yet the reader should remember that the silver target x-ray tube coupled with the DCC alone is referred to as the optical system. A comparison between the two detectors with the optical system was necessary at this stage because (1) the Zr collimated SDD has provided unsatisfactory performance and (2) because the Zr-collimated SDD was exchanged for a new multi-element collimated SDD.

The Si(Li) detector was positioned at 1 cm from the phantom, where the latter was placed at a distance 78.1 cm away from the tube to form 90° geometry (for simplicity78.1 will be referred to as 78 only). This geometry was chosen to reduce the measurement's dependency on phantom positioning as the excitation source is now an x-ray tube as opposed to a radioisotope. A closer distance was not

physically possible due to the detector's large head that would intercept with the x-ray beam. The current and voltage of the x-ray tube were set to 40 mA and 40 kV respectively. A schematic diagram of the experimental setup is depicted in figure 2.1a. Phantom spectra were acquired for 30 minutes real time and processed by the ORTEC DSPEC Plus™ multichannel analyser operating Maestro™ software and non-linear curve fitting was completed with OriginLab Pro.

Figure 2.9 shows a spectrum obtained by the Si(Li) detector in the vicinity of the Sr K x-ray peaks as well as the Ag Compton and coherent peaks. Sr K_α and K_β were fitted as two separate Gaussian functions. A linear background below the alpha peak and an exponential background below the beta peak were used as this peak was closer to the end of the Compton scatter peak. Figure 2.9 also shows a small x-ray peak at 24.9 keV, suggesting the presence of Ag K_β x-ray peak. This is not expected as the optical system should produce only monochromatic Ag K_α characteristic x-rays. To further investigate the presence of this peak, the K_α/ K_β ratio was studied.

The experimental K_α/ K_β ratio was found to be higher than the theoretical ratio by a factor of 4. This factor is expected to be higher if the Ag K_α x-rays were selected more effectively by the monochromator. Further investigation is required to confirm the minor deficiency of the DCC to select the Ag K_α x-rays only and not the Ag K_β. Moreover, phantom spectra obtained from the multi-element collimated SDD did not register the presence of the 24.9 keV peak (figure 2.11). Nevertheless, the presence of this peak at 24.9 keV did not interfere with the characteristic peaks, and therefore, it did not precluded use of the Si(Li) detector.

The direct MDL obtained from the direct K_α and K_β calibration lines were 17.14 ± 0.58 µg Sr/g Ca and 73.27 ± 5.63µg Sr/g Ca respectively. The combined MDL was thus 16.70± 0.33 µg Sr/g Ca, where the combined MDL is weighted as:

$$\frac{1}{MDL^2} = \frac{1}{MDL\alpha^2} + \frac{1}{MDL\beta^2} \quad (1)$$

since the K_α and the weighted MDL are not significantly different (coefficient of variation is 1.8%), the remaining analysis for this and the following sections was simplified and thus was based on the Sr K_α peak areas and the direct Sr Kα MDLs only.

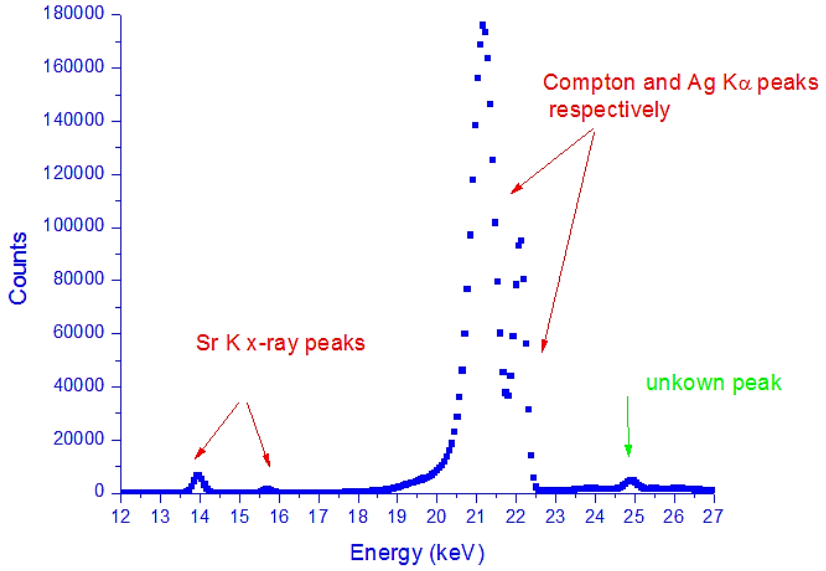

Figure 2.9: Sr phantom spectrum obtained by the Si(Li) detector from bone poP phantom of 1375µg Sr/ gCa added Sr in 90° geometry with respect to the optical system. The phantom was measured for 30 min real time.

The optical system produces Ag Kα x-rays, and thus the only two peaks pertaining to the x-ray tube is the coherent Ag Kα x-rays at 22.16 keV, along with the Compton peaks at 21.9 keV. The coherent peak was fitted in order to obtain coherent normalized Sr MDLs for a more explicit comparison of the Si(Li) detector and the multi-element collimated SDD with the optical system. Moreover, coherent normalization should correct for fluctuations in the output flux and changes in phantom positioning.

In order to fit the coherent Ag K_α peaks at 22.16 keV without cutting off counts from the lower energy end of that peak, the Compton and coherent peak had to be fitted simultaneously. First, two Gaussian functions were used to fit both scatter peaks located in the energy region from 18 keV to 23 keV. This fitting approach resulted in a poor reduced chi-square attributed to the broadened Compton peak due to Compton scatter at multiple angles and a small tail at the lower energy end due to incomplete charge collection of which both were initially neglected. Therefore, a tail function was included in the fitting routine to incorporate both phenomena (scatter at multiple angles and incomplete charge collection). Thus a third Gaussian function was added to the fitting routine, not for describing analytically the broadened Compton peak, but in order to obtain the area under it. Figure

2.10 depicts a snapshot of the fitted scatter peaks as three Gaussian functions. Once the scatter peaks were fitted, the Sr Kα peak area was divided by the coherent peak area, and the normalized MDL was extracted. Note that the Compton area in this approach is defined as the sum of the two Gaussian functions fitted for the low energy tail and the main Compton peak.

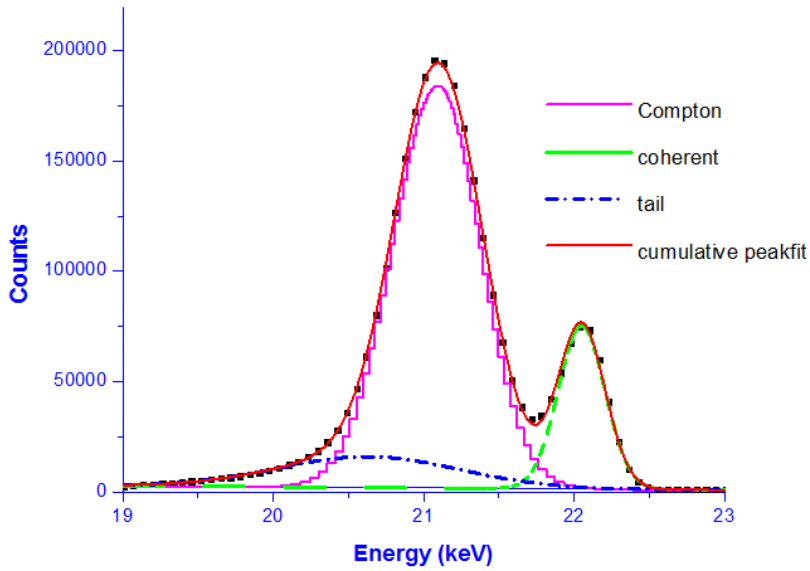

Figure 2.10: Snapshot of a sample fitted spectrum of the Compton and Ag Kα peaks using three Gaussian functions.

The normalized MDL is calculated as two times the uncertainty in the 0 ppm normalized Sr peak area divided by the slope of the corresponding calibration line. The coherent normalized MDL was 21.81 ± 0.87 µg Sr/g Ca.

After testing the performance of the Si(Li) detector with the optical system, the new multi-element collimated SDD (Ketek GmbH, Germany) was tested in the same experimental setup (figure 2.1a).

Because the multi-element collimated SDD is smaller in size than the Si(Li) detector, a closer sample to detector distance (STD) is possible. Nevertheless, in order to make a direct comparison between the Si(Li) detector and the multi-element SDD, a sample to detector distance of 1 cm was used instead. The effect of Sr signal on varying detector distances will be further discussed in the subsequent chapter. The same procedure was performed as with the Si(Li) detector and the optical system, meaning set 1 and 2 of phantom measurements were completed on day one and the third set was completed on

day two. A sample spectrum acquired from the AXAS VITUS acquisition system complementing the multi element SDD is depicted in the figure 2.11. It is important to note that the peak at 24.9 keV is not observed with the multi-element SDD as discussed previously. This does not however, eliminate the malfunction of DCC monochromator as the multi-element SDD has a lower input count rate as will be shown in section 3.4, and thus 30 minute measurements may not have been enough time to observe the Ag K_β peak. The same fitting functions were used to fit the Sr K_α, Compton, and coherent peaks as fitted when the Si(Li) detector was used in the previous section.

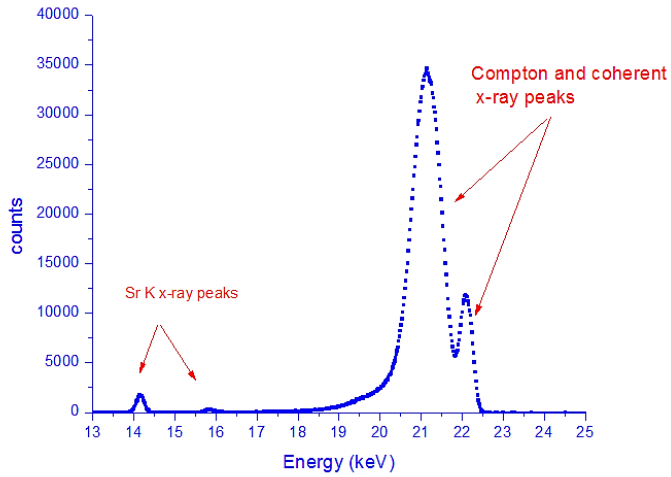

Figure 2.11: Sr phantom spectrum obtained by the multi-element SDD detector from poP bone phantom of 1375µg Sr/ gCa added Sr in 90° geometry with respect to the optical system. The phantom was measured for 1800s real time.

Table 2.5 summarizes the obtained direct and coherent normalized MDLs from two trials when either the Si(Li) detector and the multi-element SDD is used with the optical system placed in 90° geometry. For both detection systems, the coherent normalized MDL is always slightly higher than the direct MDL within uncertainty. The higher MDL is due to the added relative uncertainty in the coherent fitted peak area. Moreover, after analyzing the obtained areas pertaining to the Sr and scatter peaks, the third trial performed on the second day gave different values than trial one and two. Coherent normalization should in principle correct for flux fluctuations and changes in phantom positioning. However, the discrepancy between trials was even more apparent in the coherent peaks areas. The discrepancy between trials was also apparent in the poor linearity of the calibration line constructed from the averaged Sr and coherent normalized Sr areas. The uncertainties in the calibration line, i.e. the uncertainty in the slope and intercept including the covariance between the two, were not included in

the calculation of the MDL to follow the same calculation methods applied to the source-based Sr IVXRF in previous work. The effect of coherent normalization on phantom positioning will be discussed in chapter 4, while a method for checking changes in the output flux and a solution for detector positioning will be suggested in section 5.2 as future work.

Table 2.5: Summary of the direct and coherent normalized MDLs obtained from the Si(Li) and the multi-element SDD detector with the optical system in 90° geometry.

Experimental Conditions	Direct Kα MDL ($\mu g \frac{Sr}{g} Ca$)	Coherent Normalized MDL ($\mu g \frac{Sr}{g} Ca$)
Si(Li) +optical system	16.4 ± 0.34	19.25 ± 1.32
Multi-element SDD +optical system	13.08 ± 1.16	16.8 ± 1.53

From the sample spectra of figure 2.9 and 2.11, the superior resolution of the multi-element collimated SDD was shown to better separate the Compton and coherent peaks. At a significance level of 0.05 however, this did not result in a lower normalized MDL than that of the Si(Li) detector (p= 0.11). On the other hand, the direct MDLs obtained from both detectors were indeed significantly different (p=0.0144). These results are still not conclusive and hence selection of the detection system for the optically focused IVXRF cannot be recommended yet. Further experiments were necessary to better understand the performance of the multi-element collimated SDD; therefore a comparison of detectors' throughput using Cd-109 as the excitation source was conducted and discussed in the following section.

2.2.3 Comparison of the Si(Li)'s and the Multi-Element Collimated SDD's Throughput

Throughput is defined here as the total count rate registered and processed by a detector during its direct exposure to an x-ray/ϒ source. If the Sr peak areas obtained from the Si(Li) detector were to be divided by the Sr peak areas obtained from the multi-element collimated SDD from the previous experimental setup, the resultant ratio would be 1.97. Thus, in spite of the multi-element SDD's shorter shaping time (table 2.2), the number of counts detected from the multi-element SDD is still inferior to the Si(Li) detector, and that is possibly due to two reasons: (1)The Si(Li) detector has an active area 2.5 times larger than the multi-element SDD, and (2) the sensitive crystal thickness of the multi-element

SDD is 0.45 mm as opposed to the Si(Li)'s sensitive crystal thickness of 5.65mm, meaning that less x-rays are being absorbed in the detector.

In fact, at Sr K and Ag K x-ray energies, 30% and 72% of the incident x-rays in the detector are transmitted right through the multi-element SDD and are thus not detected. In contrast, these transmission probabilities are only 1 and 2% for the 5.65 mm Si crystal of the Si(Li) detector. The advantage of using the SDD with the optical system, if any, should be apparent when an excitation source is placed close to the detector, which would normally produce a high dead time.

Therefore, to test this hypothesis, the throughput or the gross count rate over the whole energy range from each detector was calculated, when a Cd-109 radioactive source with activity 454 MBq was placed right in front of the detector. This source was chosen because Cd-109 decays to Ag-109 with a 100% probability. These experiments were performed on the same day, thus no correction for source activity was required. The source to detector distance was chosen so that the source would produce a 40% dead time when the Si(Li) detector was used. This distance was measured to be 13.5 cm. The dead time recorded on the multi-element collimated SDD was only 1% at the same distance. Although the dead time from the latter was minimal, the Si(Li) produced a throughput 10.5 times higher than that from the SDD:

Gross Count Rate (Si(Li)-Cd-109 at 13.5cm): 16511.28 counts/s

Gross Count Rate (SDD)-Cd-109 at 13.5cm): 1508.68 counts/s

Once the gross count rate recorded from the Si(Li) detector was scaled down to have the same active area as that of the multi-element collimated SDD, the throughput would still be 4.4 times larger than that of the multi-element SDD. That is either due to the latter's low intrinsic energy peak efficiency at higher energies, or to its inherent 40 keV energy limit. This meant that energies from the coherent and incoherent Cd -109 ϒ photons (88 keV) were not detected by the multi-element SDD, and thus were not included in the integrated area. Therefore, the count rates under the Ag K_α and K_β peaks only should be calculated to perform a direct comparison. An energy range of 19.2-23.5 keV and 24.11-26.5 keV was selected as the range for the Ag K_α and K_β peak areas. These areas were divided by the live time to calculate the gross count rate within the range mentioned above.

Ag Kα + Ag Kβ gross count rate (Si(Li)-Cd-109 at 13.5 cm) = 14804.90 counts/s

Ag Kα + Ag Kβ gross count rate (SDD-Cd-109 at 13.5 cm)) = 1428.36 counts/s

The Si(Li) detector still detects 10.36 times more events than the multi-element collimated SDD. Again, if the Si(Li) detector was to be scaled down, the count rate in the vicinity of the Ag energy region

would still be 4.14 times higher than the SDD. This suggests that the energy limit of the SDD is not the reason behind its lower throughput.

The lower throughput could be due to the lower intrinsic peak energy efficiency at energies higher than 15 keV. This possibility is further supported by the typical absorption efficiency curves extracted for the EG&G Ortec Si(Li) detector and the VITUS SDD detector illustrated in figure 2.12.

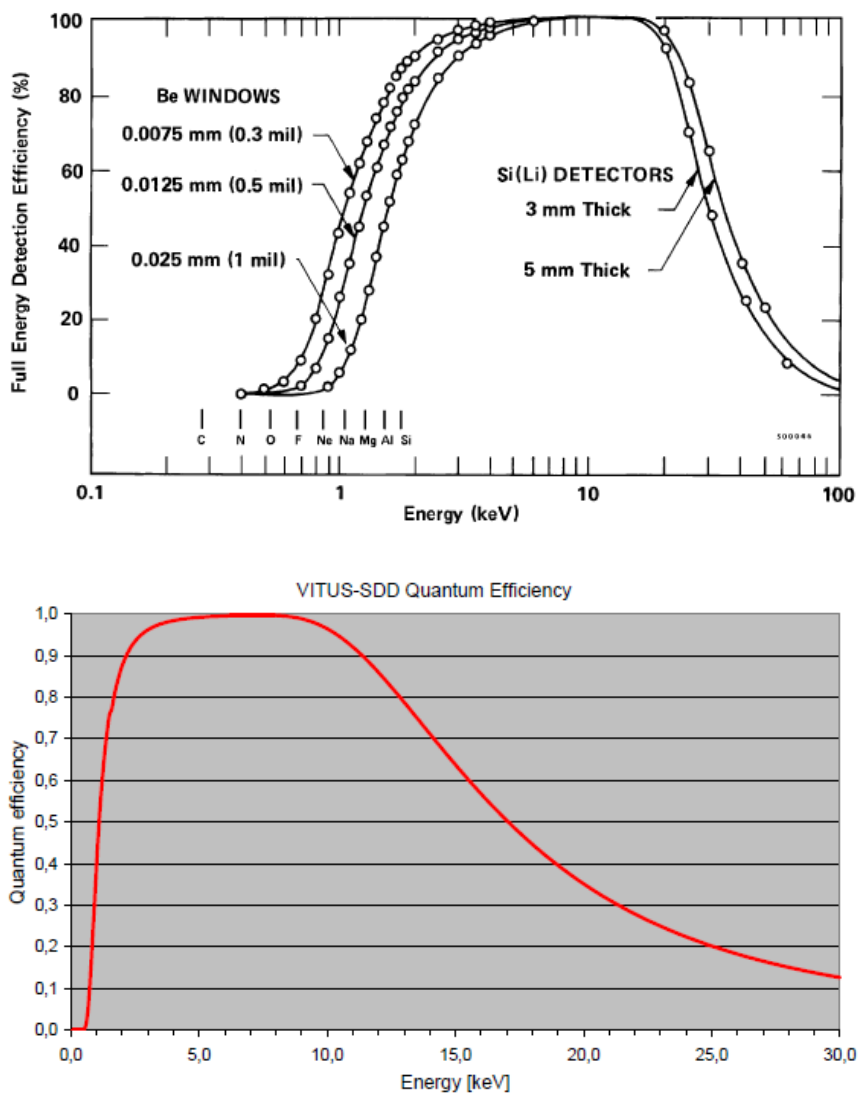

Figure 2.12: a) Absorption efficiency curve of the Si(Li) EG&G Ortec detector as a function of source energy (www.Ortec-online.com). The Si(Li) detector used in this work has a Be window thickness of 0.05mm, b) the absorption efficiency curve of the Ketek VITUS SDD (www.ketek.net) as a function of source energy. Note the quantum and the full energy detection efficiency have the same meaning as the absorption efficiency

As shown, the Si(Li) detector is more efficient to detect the characteristic Sr x-rays (~ 99%) and the incident Ag x-rays (~ 70%) than that of the VITUS SDD (~ 70% and 30% respectively).

This chapter compared the two detector's sensitivity on the source-based system and the optically focused IVXRF system according to detection limits. Gross output counts rates were analyzed to compare each detector's pulse processing capabilities at high input count rates. The results presented here suggest that from a technical point of view, the Si(Li) detector is superior to the multi-element collimated SDD. Yet, the multi-element SDD was not put to its full potential as the detector could be positioned at a closer distance to the phantom. In addition due to the limited size of the Plexiglas box the system is inserted in, different measurement geometry setups can only be tested with the smaller multi-element SDD, and thus was tested with the optical system to further investigate optimal parameters to run the optically focused IVXRF system, as presented in the next chapter.

Chapter 3 Additional Steps toward Optimizing the Optically Focused IVXRF

The absorption efficiency curves and the calculated throughput from the Si(Li) and multi-element collimated SDD detector discussed in the previous chapter illustrate that the Si(Li) detector is a better choice to use for our application, measuring bone Sr via x-ray fluorescence using the optical system set at 90° geometry. However, the multi-element SDD's small physical size makes it desirable to test different geometries, different sample to source distances, and closer sample to detector distances. In addition, the multi-element SDD is Peltier cooled, i.e. it operates without liquid nitrogen cooling, making this detector more attractive in a practical perspective. Therefore, a detailed analysis of changing the sample to source distance, sample to detector distance, and source-sample-detector geometry with the multi-element collimated SDD will be discussed as the next steps of the system development. To cap off this chapter, a summary of the parameters optimal for *in vivo* measurements with the optically focused IVXRF system will be recommended.

The signal to noise ratio (S/N) was chosen as the parameter to select the final sample to source distance that would best produce accurate results. This parameter was also chosen for studying different sample to detector distances as well. The S/N is defined here as the net peak area under the Sr K_α peak divided by the error in that area due to a very low background observed by the multi-element collimated SDD.

3.1 Evaluation of the Sample to Source Distance

For each distance, the poP phantom with the added Sr concentration of 1375 µg Sr/g Ca (labelled 2ppm) was fixed by a plastic holder with the multi-element collimated SDD and placed at 90°

with respect to the incident beam (same as previous experimental setup, see figure 2.1). The phantom was measured for 500 s real time three times at each distance. Spectra were acquired and processed from the AXAS-VITUS acquisition system along with its digital pulse processing unit accompanying the multi-element SDD. The Sr Kα peak was fitted as a Gaussian function with a linear background by using the non-linear curve fitting program in OriginLab Pro. The distances tested were 50, 62.8, 70 and 78 cm, because perfect alignment of the phantom with the x-ray beam was completed at those distances.

The S/N ratio is observed to decrease linearly with farther distances due to the increased loss of the incident photons that are either not even scattered by the poP or that are scattered by poP and are not collected by the detector due to its small active area. Although the last two distances, 70 and 78 cm were shown in section 2.2 to be the most relevant sample to source distances for IVXRF measurements, it is important to test closer distances to characterize the beam's intensity with distance first, then check if the S/N ratio varies significantly between the two distances of interest: 70 and 78 cm. It was observed that the S/N ratio obtained for all distances were highly dependent on phantom positioning, hence the large error bars. A sample to detector distance of 0.6 cm was kept constant throughput these experiments. As shown in figure 3.1, the S/N ratio at 70 cm is not significantly different from the S/N ratio at 78 cm within uncertainty ($p > 0.05$). Thus a thorough comparison between the two distances was made by means of detection limits.

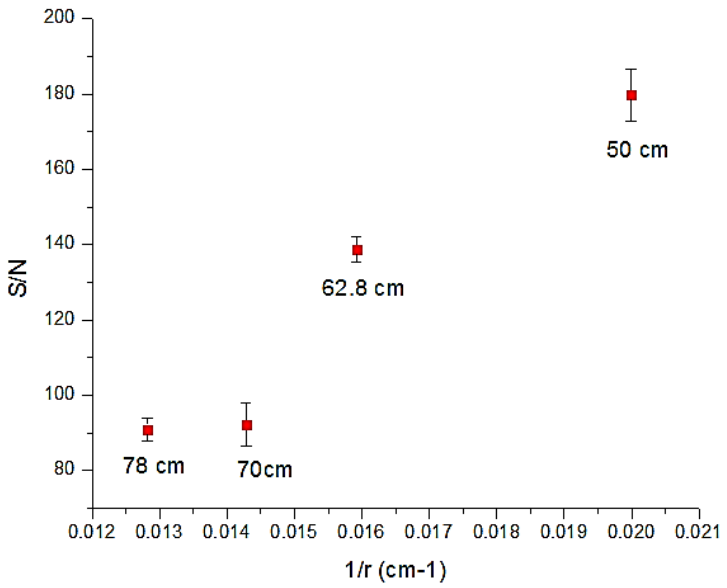

Figure 3.1: The S/N ratio as a function of inverse source to sample distance r. The uncertainty is the standard error from three trials, each trial lasted 500s.

3.1.2 Minimum Detection Limits at a Source to Sample Distance of 70 and 78 cm

For the two distances, six Sr-doped poP phantoms were measured twice, at random sequence for 30 minutes of real time. The multi-element collimated SDD was positioned at a sample to detector distance of 0.6 cm in 90° geometry. Data was acquired and processed using the AXAS-V acquisition system. With OriginLab Pro software, the Sr K_α peak was fitted as a Gaussian function above a linear background. After constructing a calibration line, the direct K_α MDL was obtained. The resultant direct K_α MDLs averaged from two trials is summarized in table 3.1.

Table 3.1: Comparison of the direct K_α MDLs from a sample to source distance of 70 and 78 cm with the multi-element SDD detector in 90° with respect to the source and phantoms.

Sample to source distance	Direct Sr K_α MDL (µgSr/gCa)
70 cm	11.48 ± 1.68
78 cm	10.37 ± 1.27

As shown in table 3.1, the direct Kα MDL at both distances is similar within uncertainty, thus agreeing with the S/N ratio measurements ($p > 0.05$). This is counterintuitive, since the S/N ratio differs by 1.3%, while the difference in the beam's spot size from 70 to 78 cm is 12%. Based on table 2.1, the beam spot at 78 cm, is only slightly wider than the spot size at 70 cm, but it is longer in the vertical direction. Therefore the longer beam spot may compensate for the loss of photons horizontally as the poP housed in the plastic tube is 0.75 cm wide, while the beam spot is 1.15 and 1.17 cm wide and 0.88 and 1.1 cm long at 70 and 78 cm respectively. Hence, the indifference between the obtained S/N ratios and MDLs suggest that both distances could be used for IVXRF measurements.

3.2 Evaluation of the Source to Detector Distance

As mentioned earlier, the closest sample to detector distance possible is 0.6 cm, as a closer distance will cause the detector's head to intercept with the incoming x-ray beam. Therefore, the multi-element collimated SDD was positioned at distances ranging from 0.6 to 4.5 cm from the poP. The sample to detector distance is defined as the distance from the plastic container holding the bone phantom to the detector's entrance window. The multi-element SDD detector was placed at 90° with respect to the phantom and the optical system (figure 2.1a). Measurements were performed on one phantom, 1375 µg Sr/g Ca of added Sr, three times for 500 s real time per measurement. According to figure 3.2, the Sr signal decreases linearly as an inverse squared distance as expected theoretically. The sharpest drop in Sr signal is observed when moving from a sample to detector distance of 0.6 cm to 0.8 cm, which supports the observation that phantom measurements have been highly dependent on positioning, especially with the multi-element collimated SDD due to its small entrance window. Nevertheless, 0.6 cm was chosen as the optimal sample to detector distance due to its higher signal to noise ratio compared to farther detector distances (table 3.2).

Table 3.2: Signal to Noise Ratio of the Sr peak at different sample to detector distances. The Sr phantoms were positioned at 70 cm away from the optical system.

Sample to Detector distance (cm)	S/N
0.6	92.20
0.8	70.59
1	54.56
1.2	49.81
2	43.17
2.5	32.55
3.5	25.04
4.5	22.18

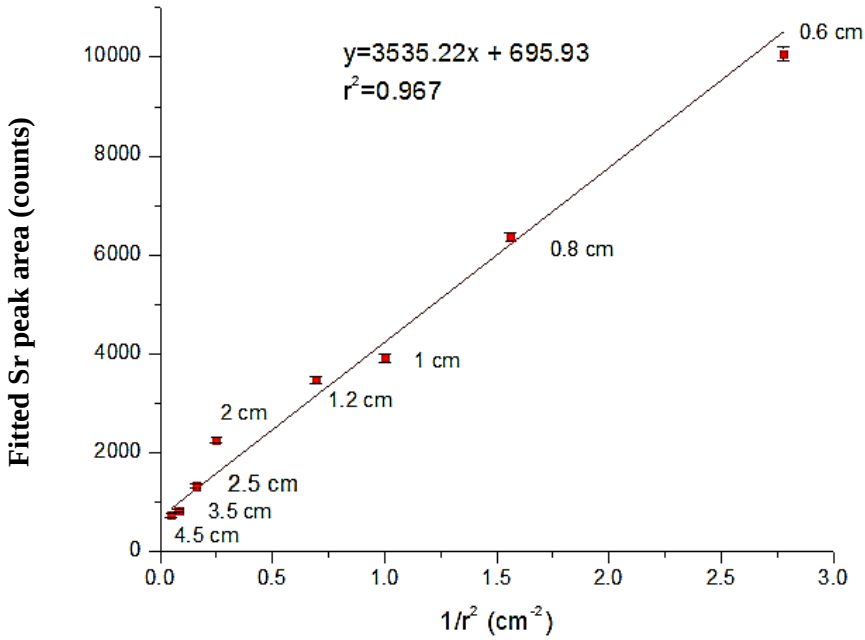

Figure 3.2: Plot of Sr Kα peak area as a function of inverse squared sample to detector distance ($1/r^2$). The error bars are the associated statistical error under the fitted Sr peaks.

3.3 Investigation of the Source-Sample–Detector Geometry

To further optimize the optically focused IVXRF system, different measurement geometries were investigated. It is important to remind the reader that 180° geometry between the detector and the source sample is used for the source-based IVXRF system (figure 1.2a). Changing the angle formed between the source-sample and the detector has an effect on the detection limit, accuracy, and reproducibility. Zamburlini and colleagues (2006) observed a lower background under the Sr peaks when the detector and source-phantom were positioned at 90° due to the farther Compton scatter peak's position from the Sr K x-ray peaks, as opposed to the 180° geometry. Typically, a lower background translated to a lower detection limit, however in the case of *in vivo* measurements, subject positioning was much more reproducible when the I-125 brachytherapy seeds were collimated and mounted on the detector in backscatter geometry, resulting in an MDL only slightly worse than that from a 90° geometry measurement (Zamburlini *et al.,* 2006). Another advantage for moving closer to 180° is that the Compton and coherent scatter peaks are more separated, improving curve fitting for the Compton and coherent peaks, and thus improving the normalized MDLs.

In this work, geometries between 90° and 180° were investigated for the optically focused IVXRF system only using the multi-element collimated SDD. The use of the Si(Li) detector was not possible due its large physical size. The closest angle possible to 180° without having the detector's neck intercepting the beam was 152°, such that the sample to detector distance was 1 cm from the phantom. Besides the 152° and the 90° geometry, 135° and 120° were tested with the same detector distance. Data was acquired using the AXAS–V acquisition system for 500 s, and the 1375 µg Sr/g Ca Sr doped poP was measured three times at each angle.

The effect of increasing angle on separating the scatter peaks is demonstrated in figure 3.3a. The effect of increasing scatter angle on the Sr signal is also shown in figure 3.3b. The Sr x-ray peaks are observed to be isotropic at all three angles except at 152°, indicating a misalignment between the detector and the phantom. In addition to this problem, the area under the Compton peak as a function of increasing scattering angle was plotted and a sudden drop at 152° was also observed. This observation contradicts theory as the Compton signal should have its maximum at 180°.The same observation was seen for the coherent signal.

Based on the obtained results, it can be concluded that an angle of 135° is large enough to fully separate the Compton peak from the coherent peak. However, because sample positioning or subject positioning at such geometry is not straightforward, the precision of an *in vivo* measurement at this angle is questionable. Reproducible and comfortable subject positioning is one of the main advantages in adopting the backscatter geometry on the source-based system, however, since 180° geometry is not feasible on the optically focused IVXRF system, this advantage is lost. Nevertheless, moving toward 135° geometry may still improve normalized MDLs, and thus a full set of phantom measurements at 135° geometry with an improved positioning technique, is recommended in the future.

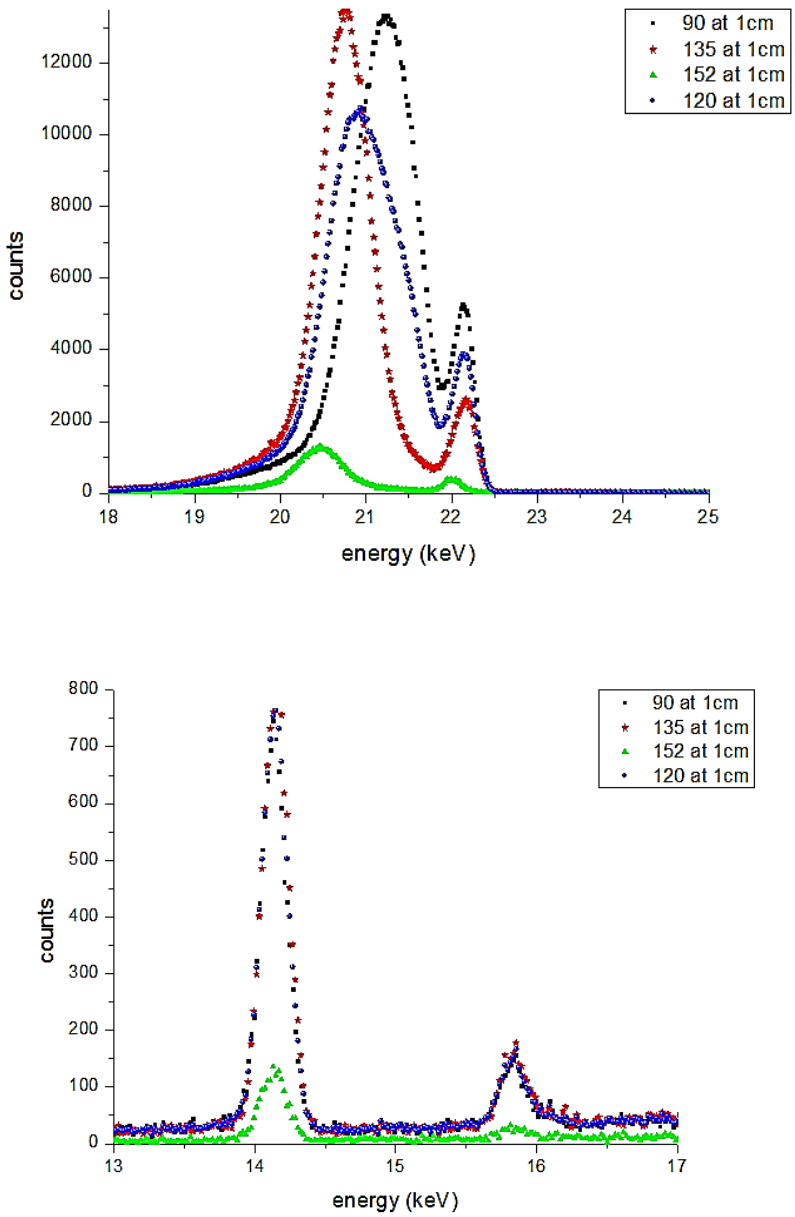

Figure 3.3: a) Sr doped poP spectrum of the Compton and coherent scatter peaks at scattering angles ranging from 90° to 152°, b) Sr doped poP spectrum of the characteristic Sr x-rays at scattering angles ranging from 90° to 152°.

3.4 Recommendation of Setup and Running Parameters for the Optically Focused IVXRF System

As shown in this work, energy resolution affects the quality of peak fitting the scatter peaks to obtain only marginally lower normalized MDLs (table 2.5). As for the S/N ratio, it was calculated as the

area under the Sr peak divided by its statistical error when the Sr doped poP was placed at 78 cm from the tube and 1 cm away from either detector. The S/N was found to be 125 and 137 when the Si(Li) and the multi-element SDD detector were used respectively, suggesting the use of the multi-element SDD will result in lower detection limits and better precision for Sr IVXRF measurement. In the previous chapter, the performance of the Si(Li) and the SDD detectors (Zr collimated and multi-element collimated SDD) with three different excitation sources and three different geometries: I-125 brachytherapy seeds in backscatter geometry, the optical system in 90° geometry, and Cd-109 in 0° was presented. However, experiments pertained to all three setups showed that under the same experimental conditions, the multi-element SDD does not outperform the Si(Li) detector. A detailed summary of the Si(Li) and the multi-element collimated SDD's properties and data collected from phantom measurements with the optical system is tabulated in table 3.3. The Si(Li) detector's larger active area has the potential to collect more x-rays than the multi-element SDD's active area, yet the real metric of x-ray detection is the solid-angle subtended by the detector. The solid-angle subtended by the detector's active window was calculated as follows:

$$\Omega = \frac{Active\ area}{(sample\ to\ detector\ distance)^2} \quad (1)$$

For the same experimental conditions (measurement geometry and detector distance), the solid angle was found to be 2 sr and 0.8 sr for the Si(Li) and the multi-element SDD respectively.

On the other hand, the direct Kα MDL obtained from the multi-element detector at sample to detector distance of 0.6 cm is significantly lower than the MDL obtained from the Si(Li) detector at an sample to detector distance of 1 cm ($p < 0.05$), where both detectors are positioned in 90° geometry and the phantoms are placed at a sample to source distance of 78 cm. Moreover, at a detector distance of 0.6 cm from the phantom, the solid angle subtended by the multi-element collimated SDD is: Ω= 2.2 sr, which is slightly larger than the Si(Li) detector's solid angle. Unfortunately, a sample to detector of 0.6 cm was not possible for the Si(Li) detector due to its larger size. Moreover, when the multi-element SDD is positioned at 78 cm away from the tube at 90° geometry, but at a detector distance of 0.6 cm instead of 1 cm, the S/N ratio under the Sr peak is 185.5. The higher S/N ratio pertained to the SDD at both distances (1 and 0.6 cm) is attributed to the lower background, since the total capacitance is much smaller for an SDD as compared to a Si(Li) detector, which minimizes the electronic noise.

To further explore differences between the two silicon detectors, the absorption efficiency was used, where absorption efficiency calculations are based on the fraction of photons traversing each detector and being absorbed in it. These efficiencies were calculated based on each detector crystal thickness (section 2.2.3). The calculated absorption efficiencies indicate that the Si(Li) detector is more sensitive to Sr and Ag x-rays (figure 2.12). An additional advantage of the Si(Li) detector, with its pulse processing unit used for the source-based system, is that the detector's operating peak parameters, such as peak rise time can be optimized according to one's application. Rise Time, Cusp width, Flat-top, and Tilt peak are peak shaping parameters previously optimized by Pejović-Milić (2001) for the source based system. Moreover, as noted by the dead times recorded for each detector in table 3.3, the shorter pulse shaping time of the multi-element collimated SDD, is not exploited as the incoming number of photons reaching the detector is very low at the 90° geometry. In fact, it has been observed that under the same tube voltage and current, the input count rate at a scattering angle of 90° is 100 times less than if the detector was positioned in front of the tube instead of the sample at a distance of 70 or 78 cm.

Based on the above discussion and on the detection limits measured by both detectors on the optically focused system at the same sample to detector distance and source to sample distance (table 2.5), although the normalized detection limits when either detector was used with the optical system are not significantly different, the Si(Li) detector is more sensitive to x-rays at energies higher than 10 keV. Moreover the Si(Li) detector subtends to a larger solid angle than the multi-element SDD at the same sample to detector distance. However, at the closer distance of 0.6 cm only possible with the multi-element SDD, the detection limit is reduced, and the solid angle subtended by the detector is slightly larger. Furthermore, a measurement geometry of 135° is recommended for more accurate fitting, but only after the SDD is fixed to the base of the shielding box, where the SDD should be placed 0.8 cm away from the sample.

In summary, although the multi-element collimated SDD has an active area smaller than the Si(Li) detector by a factor of 2.5, the solid angle subtended by the detector is comparable to the Si(Li) detector when the SDD is positioned at a distance of 0.6 cm away from the sample. Although lowering the system's detection limit from 17 to 10 µg Sr/g Ca is not crucial for bone Sr IVXRF measurements, the MDL along with its error should give an indication on the precision and accuracy of each experimental setup. It was observed that the multi-element SDD's reproducibility was compromised at a sample to detector distance of 0.6 cm. Nevertheless, if the detector positioning is the only factor compromising

the system's reproducibility, than pinning it down as suggested earlier should improve the precision remarkably. However, more is required to address this further. A summary of the parameters recommended for the optically focused IVXRF system is tabulated in table 3.4.

Table 3.3: Summary of the Si(Li) and the multi-element SDD detectors' properties suggested for bone Sr on the optically focused IVXRF system. Data for dead time and signal to noise ratio are obtained using the 1375 µg Sr/g Ca doped phantom.

Detector properties	Si(Li) detector	Multi-element collimated SDD
Active diameter (mm)	16	10.1
Peak rising time/shaping time (µs)	10	3
Detector thickness (mm)	5.65	0.450
Energy resolution at 14.2 keV (eV)	290	225
S/N under Sr K_α peak (30 min counting)	125	137
Solid angle at detector distance of 1 cm (sr)	2	0.8
Transmission Efficiency (%) at 22.2 keV	2	72
Dead time (%)	1.8%	0.5%

Table 3.4: Recommended sample to source distance, sample to detector distance, and geometry

Detector	Source to sample distance (cm)	Sample to detector distance (cm)	Geometry
Multi-element SDD	78 or 70	0.6	90°
Multi-element SDD	78 or 70	0.8	135°

Chapter 4 Investigation of Different Normalization Techniques for bone Sr IVXRF

Although XRF measurements are straightforward for qualitative analysis, quantitative XRF analysis on the other hand is not. In the case of bone Sr IVXRF, bone as a sample is not considered thin nor is it mono-layered, but it is considered infinitely thick as 99% of Sr K_α x-rays will be attenuated by 2.26 mm of cortical bone and 99% of Sr K_β will be attenuated by 3.1 mm of bone. For this reason, creating a calibration line relating fluorescent x-ray intensities to known [Sr] from external standards, such as poP, is a necessary first step to obtain [Sr] in human bone.

Prior to converting the number of detected x-rays to [Sr], several experimental and geometrical factors should be corrected for. Experimental factors comprise of source strength, source and detector size and collimation, measurement duration and subject movements during a measurement to name the most important factors. Geometrical factors include source subject and subject detector distance, bone size, and variable overlying soft tissue thickness. Some of these quantities cannot be readily obtained, such as the subjects' bone size and overlying soft tissue thickness, and therefore an alternative approach is desirable. Coherent normalization is one of the suggested approaches, where already available information in the obtained *in vivo* spectrum is used to correct for or at least simplify the confounding factors pertained to an IVXRF measurement (Somervaille *et al.*, 1985). Incoherent scatter on the other hand, has been widely used as an internal standard for geological and biological samples or as a correction to account for the difference in the absorption between the analyte and the external standard used (Verdurment *et al*., 1977; Giauque *et al*., 1979).

This chapter describes the theoretical justification behind possible normalization techniques investigated, followed by a couple of experiments, testing the feasibility of each for bone Sr IVXRF using the optically focused IVXRF system.

4.1 The Feasibility Study of Coherent Normalization for the Optically Focused Bone Sr IVXRF System

Coherent normalization has been adopted to IVXRF measurements of bone lead and bone uranium (Somervaille *et al.,* 1985; O'Meara *et al*., 2001; O'Meara *et al*., 1998). Somervaille and colleagues (1985) were the first to realize that the x-ray to coherent ratio is directly proportional to bone Pb concentrations in the Cd-109 source-based IVXRF system applied in the backscatter geometry, and that it is independent of geometrical and experimental factors. In principle, coherent normalization is feasible if the following conditions are satisfied: (i) The characteristic x-rays and coherent photons are produced by the same incident fluence; (ii) Both signals originate from the same region in the measured sample; (iii) Both signals have the same angular distribution, and finally (iv) the x-rays and coherent photons are attenuated in the sample in a similar way. In the Pb K x-ray IVXRF system, the excitation source used is Cd-109 ϒ photons and is placed in 180° geometry with respect to the sample. Coherent normalization works perfectly because all four conditions are satisfied (see section 1.4). For the Pb K x-ray IVXRF system where Co-57 is the excitation source positioned in 90° geometry with respect to the finger bone, coherent normalization was shown to correct for subject movements and bone size within 5-10% of the mean ratio over the entire range of soft tissue and bone radii relevant for *in vivo* measurements, despite not strictly satisfying the above conditions. In addition, the x-ray to coherent ratio was shown to be less variable with increasing soft tissue thickness than the x-ray intensities alone (O'Meara *et al*., 2001).The validity of coherent normalization without having all the aforementioned conditions satisfied was explained to be due to some compensation between the quantities involved (O'Meara *et al.,* 2001). Normalizing the x-ray signal to the coherent signal was experimentally tested by varying the poP bone size at a constant tissue thickness and phantom to detector distance first, then varying the soft tissue thickness (Perspex) surrounding the bone phantom with a constant phantom radius, while keeping a constant sample to detector distance. These experiments were complemented and verified by Monte Carlo simulations (O'Meara *et al*., 2001).

As for the Sr bone I-125 based IVXRF, Monte Carlo simulations and experiments analogous to the tests performed on the Co-57 based Pb IVXRF system showed that coherent normalization by the 35.5 keV ϒ photons corrected for bone size within an accuracy of 10% of the mean ratio, but not for signal attenuation by the overlying soft tissue. To compensate for this partial normalization, a separate

means to correct for the Sr attenuation in soft tissue has been applied, such as using ultrasound imaging (Zamburlini *et al*., 2008)

Prior to the I-125 based bone Sr XRF system, Ag x-rays from Cd-109 radioactive source was used to excite Sr in 90° geometry (Pejović-Milić *et al*., 2004). Their experimental setup was similar to the x-ray tube based system described in this work, where the optical system produces Ag K_α x-rays and the detector was placed in 90° with respect to the source and sample. The Ag K_α coherent peak is closer to the Sr x-ray energies than I-125, and is thus more efficient in exciting Sr atoms, however Sr x-rays can still be excited by Ag Compton x-rays, and hence condition (i) for coherent normalization is not satisfied. 99% Sr x-rays arise from bone but, Ag x-rays arise from soft tissue and bone together as the differential coherent cross section in bone is only 1.8 times higher than in soft tissue. Hence condition (ii) is not fulfilled. Moreover, the angular distribution of the coherent x-rays is anisotropic near the 90° scattering angle, while Sr x-rays are isotropic for all scattering angles equal to and larger than 90°, thus condition (iii) is not satisfied as well. Condition (iv) is not fulfilled, because at these low energies the source photons and Sr x-rays have different attenuation properties in bone and soft tissue (table 1.3). Nevertheless, Monte Carlo simulation for the Cd-109 source based Sr IVXRF system showed that coherent normalization does correct for changes in bone size within 20% of the mean Sr to coherent ratio (Pejović-Milić *et al*., 2004). On the other hand, it did not correct for the overlying soft tissue attenuation, but in fact caused the normalized signal to be more dependent on tissue thickness. That is owing to the fact that more coherent x-rays will originate from soft tissue with increasing tissue thickness, while the Sr x-ray signal decreases under this condition. Following the reason that several cancelling factors in coherent normalization still give rise to x-ray to coherent scatter ratio that could be invariant to geometrical and experimental factors, the feasibility of coherent normalization was tested experimentally for the optically focused IVXRF system developed in this work.

Under the same tube voltage and current, the tube's flux should not in principle vary between measurements. The poP bone phantoms used to calibrate and optimize the system all had the same bone diameter of 0.8 cm and are cylindrical in shape. They were aligned with the exiting x-rays by beam imaging at several distances as discussed in section 2.1, and then positioned using a plastic sample holder fixed to the base of shielding box. In addition, bone phantoms of different radii were not available at this time. However, overlying soft tissue mimicking tubes, Perspex, were readily available with the plastic thicknesses ranging from 1.5mm to 4 mm. This range encompasses the range of expected human soft tissue thickness overlying the phalanx finger used for human measurements.

The 1375 µgSr/ gCa Sr-doped poP phantom mimicking bone was inserted in the plastic tube and was placed at 70 cm away from the optical system. The plastic holder and the poP together were repositioned after each measurement with a constant sample to detector distance of 0.6 cm. This meant that with increasing plastic tube thickness, the distance between the detector and the poP increased in steps of 0.5 mm in addition to the extra 0.65 mm of Perspex that holds the bare bone phantoms. For each thickness, the covered phantom was measured three times for 500 s real time. Data was acquired and processed using the AXAS- V acquisition system. Nonlinear curve fitting was applied using OriginLab Pro software, where Sr Kα x-ray peaks and the coherent Ag Kα peaks were fitted separately as a Gaussian function above a linear background. The Sr Kα signal and the coherent normalized Sr signal are both shown in figure 4.1a and 4.1b. As expected, both signals decrease sharply with increasing plastic thickness.

These results are in agreement with the findings of Pejovic`-Milic` *et al*. (2004) for Ag Kα coherent normalization of the Sr peak on the Cd-109 based XRF system set in 90° geometry. They are in agreement as well with the conclusions from Zamburlini and colleagues (2008) when the I-125 or Ag Kα coherent normalization of the Sr peak on the I-125 based XRF system set in 180 ° was used. Since, the coherent normalization has been reported to reduce the measurement's dependency on subject movements during a single measurement (Zamburlini *et al.,* 2008; O'Meara *et al.,* 2001), and since the signal to noise ratios and detection limits extracted were shown in the previous chapter to be highly dependent on sample and detector positioning, this normalization was put into test.

The 1375µg Sr/g Ca Sr doped poP was inserted in the sample holder fixed at 70 cm away from the optical system. The multi-element collimated SDD was then positioned in 90° with respect to the poP at distances ranging from 0.6 cm to 3.5 cm. These measurements were performed on the same phantom three times for 500 s real time. The effect of increasing detector distance on the Sr Kα signal with and without coherent normalization is illustrated in figures 4.2a and 4.2b.

a)

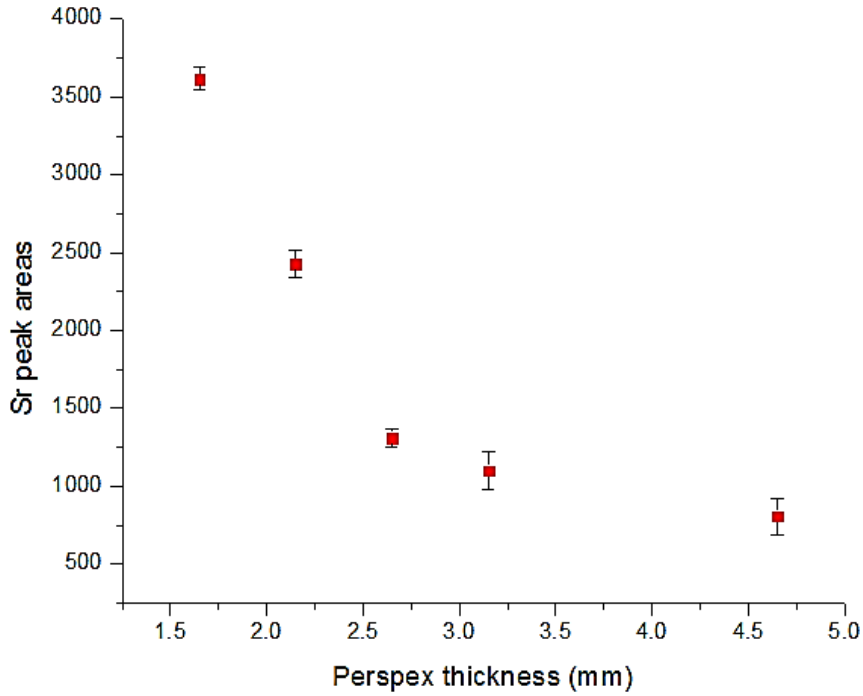

b)

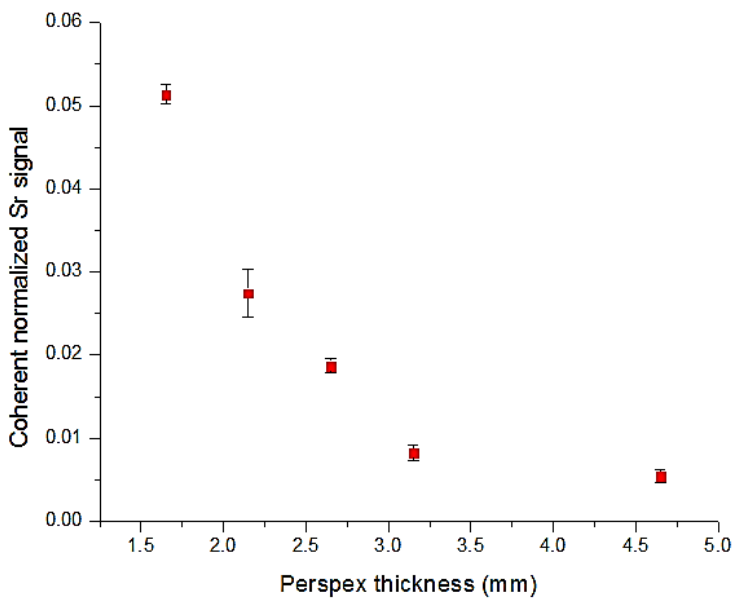

Figure 4.1: a) Sr Kα peak areas of Sr doped poP phantoms as a function of the soft tissue mimicking thickness overlying poP b) Coherent normalized Sr Kα peaks as a function of the tissue mimicking thickness. The error bars pertain to the statistical error from three measurements, 500s real time. Data was collected using the optically focused bone Sr IVXRF system in 90° geometry.

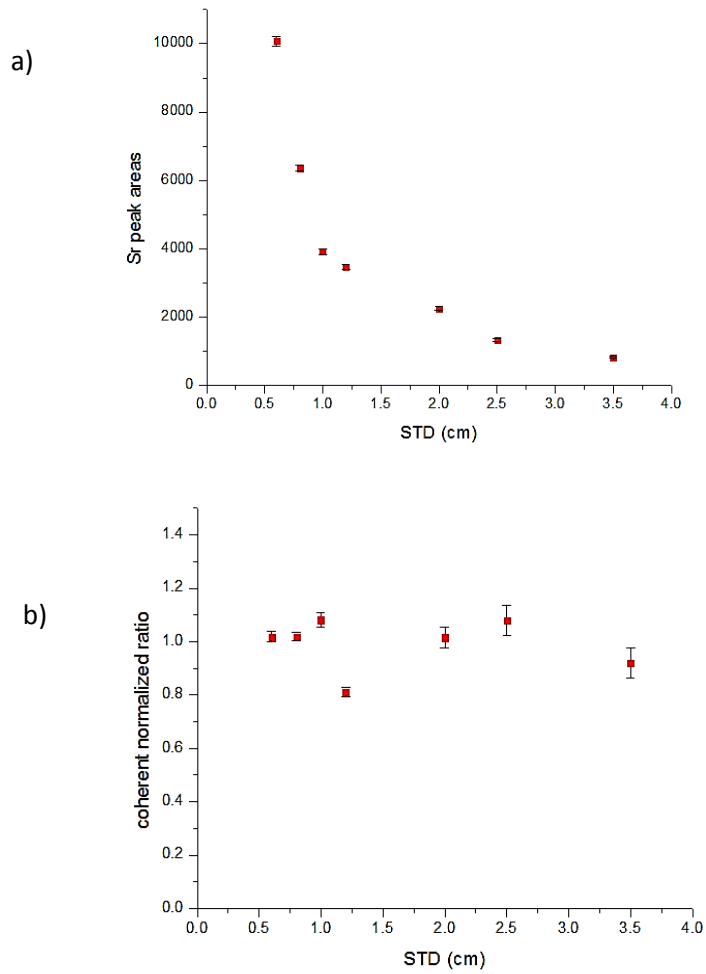

Figure 4.2: a) Sr Kα peak areas from Sr doped poP phantoms as a function of sample to detector distance (STD), b) Coherent normalized Sr Kα peaks as a function of sample to detector distance (STD). Note that the coherent normalized areas were scaled to the average area. The error bars in both figures are the statistical errors from three measurements, 500 s real time. Data was collected using the optically focused bone Sr IVXRF system in 90° geometry.

Even though a subject will not typically move his finger 3 or 4 cm from its original position, the fact that the normalized Sr areas do not vary considerably with the sample to detector distance support the hypothesis that coherent normalization improves the overall accuracy of an XRF measurement. The coefficient of variation (COV) from the mean x-ray to coherent ratio was found to be 9.6%, which is comparable to the COV of 6.7% obtained from testing coherent normalization on the source-based system with the 35.5 keV coherent peak (Zamburlini, 2008)

4.2 Feasibility Study of Incoherent Normalization for the Optically Focused Bone Sr IVXRF

Geological samples vary in composition and thus, a calibration internal standard with similar x-ray properties to the analyte and not present in the original sample are added to the measured sample. However, for multiple elemental analyses, selecting, accurately weighting and homogenously mixing internal standards become a challenge. Instead, it was proposed that the intensity of the primary radiation scattered from the sample can be used as an internal standard (Andermann and Kemp, 1958). Reynolds (1963) on the other hand, was the first to use the incoherent scatter intensity to determine the total mass attenuation coefficient of a sample of unknown composition, and then use the ratio of the mass attenuation coefficient of one external standard to that of the sample in order to correct for the difference in absorption properties between the sample and the standard. In fact, it was shown by Kalman and Heller (1962) that the fluorescent to scatter radiation ratio (the continuous scattered radiation originated from an x-ray tube, or more often the incoherent scatter only) should in principle be independent of sample composition, excitation conditions, sample size and other experimental variations, if the following conditions are satisfied:

1. No major element has an absorption edge between the energies of the fluorescent and the scatter, the incoherent and coherent, peaks.
2. Scattered x-rays and fluorescent x-rays have similar energies.
3. Other elements in the sample shall not enhance the fluorescence of the element of interest
4. The sample is composed mainly of low Z elements.

Although no IVXRF measurement reported the use of incoherent scattering as a means for signal normalization, it was tested in this work for three reasons: (1) The monochromatic nature of the optical system and the superior resolution of the multi-element collimated SDD allowed the incoherent peak to be separated enough for accurate fitting and area extraction, (2) quick analysis of the relative error in the fitted area under the incoherent peak from the multi-element collimated SDD was found to be an order less than the relative error for the coherent peak, which should in turn translate to a lower detection limit compared to the coherent normalized MDL, and (3) for the present experimental setup and under the above conditions, the fluorescent to incoherent intensity ratio can be shown theoretically to be matrix independent, i.e. inter-element effects are negligible as demonstrated below.

In bone Sr IVXRF, Ag x-rays of energy 22.16 keV is the primary incoming beam and Sr is the targeted

atom with absorption edge 16.20 keV present in bone. The energy difference between Sr Kα x-rays and the scattered Ag x-rays range from 7 keV for incoherent scattered x-rays (at 90° scattering angle) to 8 keV for coherently scattered Ag x-rays, thus satisfying condition 2. Sr is a minor element of high Z typically present in bone mineral, and so no major source of characteristic x-rays from other elements present can cause Sr excitation or have an absorption edge between Sr and Ag x-rays, hence conditions 1 and 3 are also satisfied. Condition 4 is satisfied as well, since the major elements constituting bone are Ca, C, P and O. It is important to note that some higher Z trace elements such as Pb, Cd, and U are accumulated in human bone, however for the purpose of this theoretical analysis, these trace elements can be neglected.

The intensity of the fluorescent x-rays, coherent and incoherent scattered x-rays all depend on the mass attenuation coefficient. Full expression of the coherent scattered intensity is documented by Kalman and Heller (1962). The simplified expression, relevant for the discussion here, is:

$$I_{coherent} \propto \frac{U(E_i)\times\sigma_{coh}}{\mu_{s,Ei}+A.\mu_{s,Ei}} \quad (1)$$

where *U (Ei)* is the intensity of the incoming x-ray beam with energy E_i, and $\mu_{s,Ei}$ is the mass attenuation coefficient of the sample *s* at the primary, incoming, source x-ray energy E_i. σ_{coh} is the mass coherent scatter cross section at the incident energy and A is the geometrical factor defined by $\frac{sin\varphi_1}{sin\varphi_2}$, where $\varphi_1$and φ_2 are the incident angle of the primary and emergent angle of the fluorescent radiation respectively.

The simplified expression for the incoherent scattered intensity is:

$$I_{incoherent} \propto \frac{U(E_i)\times\sigma_{incoh}}{\mu_{s,Ei}+A.\mu_{s,Ec}} \quad (2)$$

where, $\mu_{s,Ec}$ is the mass attenuation coefficient of the sample at the incoherent photon energy and σ_{incoh} is the mass incoherent scatter cross section at the incident photon energy.

It has been shown that, if and only if, no major element in the sample has its absorption edge between the primary and fluorescent x-ray, the mass attenuation coefficients at the incoherent and coherent scattered energies are directly proportional to the mass attenuation at the fluorescent energy (Hower, 1959) and therefore equations (1) and (2) can be written as:

$$I_{incoherent} \propto \frac{U(E_i)\times\sigma_{incoh}}{cte\times\mu_{s,Ef}} \; or \; I_{incoherent} = \frac{P\times\sigma_{incoh}}{\mu_{s,Ef}} \tag{3}$$

$$I_{coherent} \propto \frac{U(E_i)\times\sigma_{coh}}{cte\times\mu_{s,Ef}} \; or \; I_{coherent} = \frac{Q\times\sigma_{coh}}{\mu_{s,Ef}} \tag{4}$$

As for the fluorescent characteristic x-rays, the intensity is:

$$I_{fluorescent} \propto \frac{R\times C_i}{\mu_{s,Ef}} \tag{5}$$

Parameters P,Q, and R are constants independent of matrix composition, cte is a proportionality constant, and C_i is the concentration of the element of interest. Under the conditions set above, the relationship between the mass incoherent scattering coefficient and the total mass attenuation coefficient of the elements present in the sample at the fluorescent energy of the minor element in question is approximated to be linear. For Ag K_α incoherent peaks and Sr fluorescent peaks in rock samples (Tertian and Claisse, 1982), this relationship is reported as:

$$\sigma_{incoherent}\ (\text{at } 22.16 \text{ keV}) = 0.01 - 0.00003\mu\ (\text{specimen at } \mathrm{E}_f) \tag{6}$$

Assuming the same relationship for the case discussed here and by substituting (6) in (3) yields to:

$$I_{incoherent} = \frac{P\times(0.01-0.00003\mu_{s,Ef})}{\mu_{s,Ef}} \text{ or } \mathrm{I_{incoherent}} = \frac{\mathrm{P}\times 0.01}{\mu_{\mathrm{s,Ef}}} - \mathrm{P}\times 0.00003 \tag{7}$$

where P is the same constant used in equation (3).

If the last term in (7) is deemed negligible as in the case of Sr in rock samples, then the incoherent intensity is inversely proportional to the mass attenuation coefficient only, and thus, the fluorescent to incoherent intensity ratio becomes matrix independent and directly proportional to the elemental concentration:

$$\frac{I_{fluorescent}}{I_{incoherent}} \propto C_i \tag{8}$$

Another example of the applicability of this normalization is the work of Reynolds (1963), by which he experimentally found the intercept to be negligible by plotting the incoherent Mo Kα x-rays

against the inverse of mass attenuation coefficient of pure elements and compounds common in rocks and geological samples.

Although there is no theoretical relationship between the mass coherent scattering coefficient at the incident energy and the mass attenuation coefficient at the fluorescent energy, Tertian and Claisse (1982) found theoretically, followed by experiments similar to Reynolds's, that for a minor heavy element in a mainly low Z matrix, such as Sr in rocks, the relationship is indeed linear:

$$\sigma_{coherent}\ (\text{at } 22.16\ \text{keV}) = 0.0015 + 0.00018\mu\ (\text{speciman at } \mathrm{E}_f) \tag{9}$$

Similar to the analysis for incoherent intensity, substituting (9) in (4) yields to:

$$\mathrm{I}_{\mathrm{coherent}} = \frac{\mathrm{Q}\times 0.0015}{\mu_{\mathrm{s,Ef}}} - \mathrm{Q} \times 0.00018 \tag{10}$$

The authors however found that the intercept is not negligible in this case. It follows that if this intercept is found experimentally, using a transmission technique, the fluorescent to coherent ratio will still be independent of matrix composition (Giauque *et al.*, 1979):

$$\frac{I_{fluorescent}}{I_{incoherent-intercept}} \propto\ C_i \tag{11}$$

Finding the intercept experimentally, as proposed by Giauque and colleagues (1979), is feasible only if the samples are thin, which is not the case for calibration standards or real human finger in the bone Sr IVXRF.

The conditions for Compton normalization is justified for Sr in bone, as explained before, but not for the coherent normalization; therefore this approach for peak normalization was not further studied.

Data from the experiments involving the comparison of the Si(Li) detector and the multi-element collimated SDD with the optical system described in section 2.2.2 were readily available to extract MDLs from Sr areas normalized to the Compton scatter peak. The reason is that as discussed earlier, the coherent peak had to be fitted simultaneously with the Compton peak due to their proximity in energy at 90° geometry. The direct, coherent normalized, and Compton normalized MDLs are tabulated therefore in table 4.1.

Table 4.1: Comparison of direct, coherent and incoherent normalized MDLs obtained from the multi-element collimated SDD and the Si(Li) detector with the optical system at a sample to source distance of 78 cm and a sample to detector distance of 1 cm using bone mimicking poP phantoms positioned at 90° geometry.

Experimental conditions	Direct Kα MDL (μg Sr/g Ca)	Coherent normalized MDL (μg Sr/g Ca)	Incoherent normalized MDL (μg Sr/g Ca)
Multi-element SDD +optical system	13.08±1.16	16.8±1.53	12.63±1.51
Si(Li) +optical system	16.4± 0.34	19.25±1.32	31.66 ±2.10

The relative statistical error from the incoherent or the coherent peak areas is a direct indicator of whether normalizing the Sr K_α peak area with either scatter peaks is optimal. It is important to remind the reader that this was not possible in previous work of our group, where the I-125 brachytherapy seeds produced multiple overlapping x-ray and scattering peaks. With the Si(Li) detector, the average relative error in the incoherent peak area from all added Sr concentrations was found to be 3%, while the relative error in the coherent peak area was 1%, and hence the normalized MDL to the coherent scatter peak is lower than that of incoherent normalized MDL. On the other hand, for the multi-element collimated SDD, the average relative error in the incoherent peak area was found to be an order of magnitude less than the relative error in the coherent peak area (0.1% v.s 1%), and thus the incoherent normalized MDL obtained was lower than the coherent normalized MDL. This change can be attributed to the SDD's better energy resolution than that of the Si(Li) detector improving the quality of the fit for the scatter peaks.

The above experimental results show that normalizing Sr peaks with incoherent scattering rather than coherent scattering render better detection sensitivity when the multi-element is used, while the theoretical discussion demonstrates that incoherent scatter normalization is more justifiable to obtain an x-ray to scatter ratio that is independent of the changes in matrix composition than using coherent normalization.

Theory and experiment, however do not demonstrate the efficacy of incoherent normalization to correct for experimental conditions such as signal attenuation in the overlying soft tissue and changes in sample detector positioning. Therefore, data from the experiments performed to test the usefulness of coherent normalization on detector positioning and overlying soft tissue in section 4.1 were used to further address this question. The incoherent scatter peak and the low energy tail together were fitted

as two Gaussian functions on a linear background. The areas were then added and the Sr x-ray peak was normalized by the resultant area of the incoherent peak. Figure 4.3 a) shows the effect of increasing overlying Perspex thickness on the incoherent normalized Sr signals, while figure 4.3 b) shows the effect of changes in phantom to detector distance on the incoherent normalization of Sr signal.

The same trend observed in the coherent normalized Sr signal is apparent in the incoherent normalized Sr signal, meaning that incoherent normalization does not correct for the overlying soft tissue, while it accounts for changes in detector positioning with respect to the sample. The COV of the normalized values as a function of sample to detector distance was found to be 22.4% from the mean value, which is more than twice the COV calculated from the coherent normalized values. Therefore, the incoherent normalization appears not to be superior to the coherent normalization technique.

Incoherent scattering has been more widely used in geological samples to correct for difference in absorption between the analyte and the internal standard (Verdurmen, 1977; Reynolds, 1963), or as an internal standard itself for varying matrix composition (Giauque et al., 1979; Leoni and Saitta, 1977). The latter use could be valuable for IVXRF measurements as no two fingers from two different subjects are identical in composition. However further investigation would be necessary.

For the bone Sr optically focused IVXRF system, coherent normalization seems to be the optimal normalization technique as the coherent scattering coefficient at these low energies increases rapidly with increasing Z, making the coherent normalization more sensitive to changes in the composition of bone mineral. Analogous to using the ratio of Compton scatter (or the mass attenuation) from the analyte to the Compton scatter from the external standard to correct for matrix differences between the two, it has been shown that the difference in composition between cortical bone and poP can be corrected for by taking the ratio of differential coherent cross section of each at a given excitation photon energy and scattering angle as mentioned in section 1.4 (Todd et al., 2000). Heirwegh (2008) calculated this ratio at 180° for the coherent 35.5 keV ϒ photons to be 1.91. Similarly, the poP to cortical bone differential coherent cross section ratio at Ag K_α x-ray energy and at a scattering angle of 90° is found to be 1.75.

a)

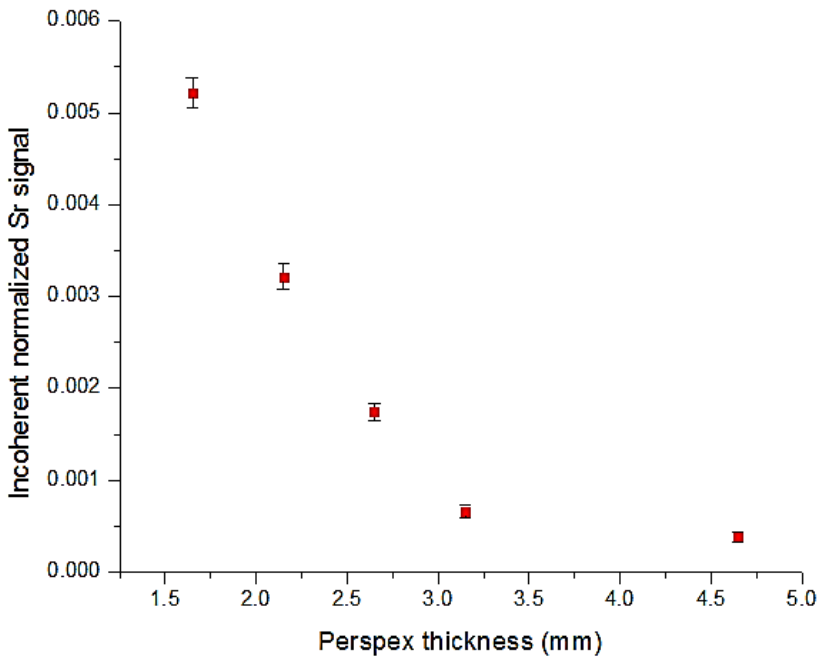

b)

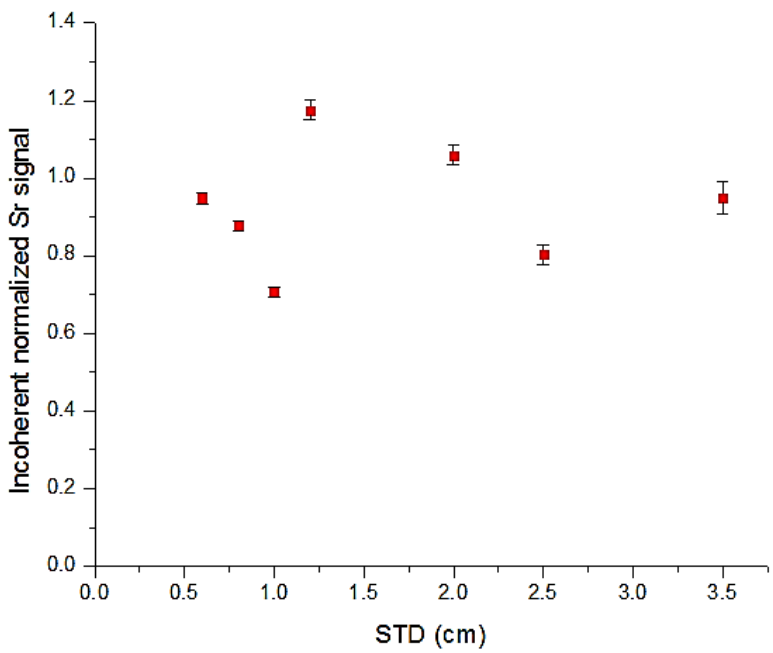

Figure 4.3: a) Incoherent normalized Sr Kα signal as a function of increasing Perspex thickness overlying the poP bone phantom, b) Incoherent normalized Sr Kα peaks as a function of sample to detector distance (STD). Note the areas were scaled to the average area. The error bars are the statistical errors associated with three measurements, 500 s real time.

4.3 Coherent to Incoherent ratio as a Means of Sr Normalization for the Optically Focused Bone Sr IVXRF

Incoherent scattering is usually used to determine the mass attenuation coefficient of a sample of unknown composition, in order to make x-ray absorption corrections between the minor element of interest and the standard used (Sitko, 2006). This method is experimentally based, where a set of samples of known compositions are used to calibrate the incoherent scatter peak as a function of mass attenuation coefficient. On the other hand, the coherent to incoherent scatter ratio is often used in an iterative approach to correct for absorption from light elements and to determine sample thickness (Neilson, 1977). Donativi and colleagues (2007) suggested that the coherent to incoherent ratio is superior from using each scatter radiation independently to gain information on the structure and physical characteristics of the samples being investigated.

The mathematical reasoning behind this normalization approach is that the coherent cross section is dependent on the physical density of the sample and the atomic number, while the incoherent scattering is dependent on the physical density alone, and thus a ratio of the two scattering intensities should be dependent on Z only and independent of the sample density or source strength. Following the same logic, the characteristic x-ray peak normalized with the coherent to incoherent ratio is then in effect not correcting for changes in excitation conditions as well as experimental positioning. This was confirmed experimentally where, the Sr signal normalized to the scatter ratio varied with increasing sample to detector distance (Figure 4.4). It was also shown that the coherent to incoherent ratio is less dependent on sample thickness (Sitko, 2006). In fact this ratio is equal to F^2/S (F is the atomic form factor and S is the scattering form factor both dependent on Z, incident energy, and scattering angle Θ) in the case of thin samples or at small scattering angles where multiple incoherent scattering is negligible (Sitko, 2006).

Although the poP phantom cannot be considered a thin sample and the scattering angle used in all experiments was 90°, the independence of the coherent to incoherent scatter ratio on sample thickness observed by Donativi and colleagues (2007) and Sitco (2006) was tested using the same data used to investigate the incoherent and coherent normalization separately. The scatter ratio was shown for the phantom measurements to be indeed less dependent on overlying soft tissue thickness than coherent or incoherent scatter separately (figure 4.5a). However, normalizing the Sr peak to

coherent/incoherent did not render the ratios to be invariant to overlying thickness, meaning that the attenuation of Sr signal cannot be overpowered (figure 4.5b).

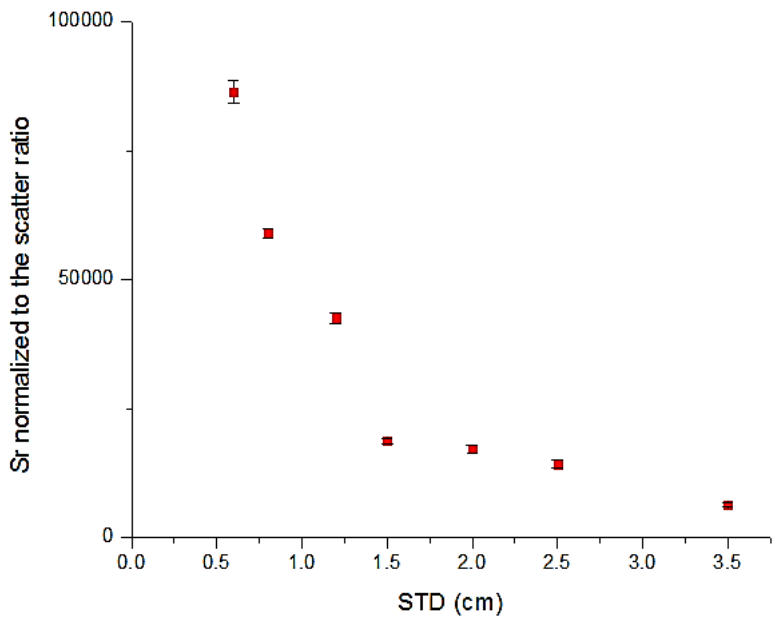

Figure 4.4: The effect of Sr Kα signal normalized to the Coherent/incoherent ratio with increasing sample to detector distance (STD). Note the error bars are the statistical error from three measurements, 500s real time.

In other applications, the scatter ratio has been used to extract structural information of the sample at hand. Kerr and colleagues (1980) found the coherent to incoherent ratio to be an indicator of bone mineral health in trabecular bone. Farquharson and colleagues (2010) found the fraction of adipose to fibrose tissue in breast tissue samples using this ratio, while Webster and Lillicrap (1985) showed that the coherent to incoherent ratio can be used to determine the effective atomic number (Z_{eff}) of pure and composite compounds, even if the specimens are thick enough for multiple scattering to be significant. The authors measured the scatter ratio of Al, simulating bone, covered with Perspex and showed that multiple scattering did not skew the direct relationship between the effective atomic number of the sample and the coherent to incoherent scatter ratio. Duvachelle et al (1999) confirmed the findings of Webster and Lillicrap, explaining that choosing the appropriate scattering angle and incident energy enables the scatter ratio to be independent of x-ray attenuation inside the sample.

a)

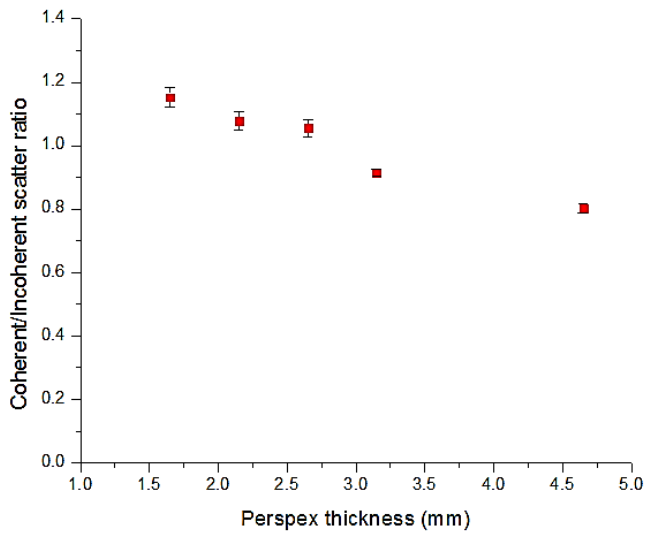

b)

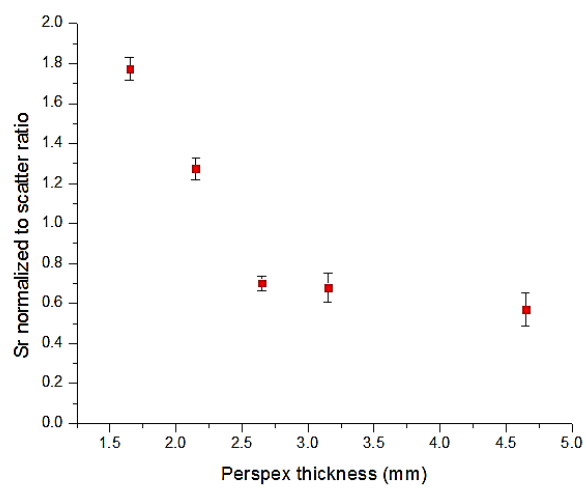

Figure 4.5a): Coherent to Incoherent ratio as a function of increasing Perspex thickness b) Sr Kα normalized to the scatter ratio as a function of increasing Perspex thickness overlying poP phantom. The ratios were scaled to the mean scatter ratio and the error bars are the scaled statistical errors from three measurements, 500s real time.

It follows that for Sr IVXRF, the coherent to incoherent ratio could be used to represent the effective atomic number that combines the effective atomic number of bone and the effective atomic number of overlying tissue. Knowing Z_{eff} of tissue and bone from literature, or from prior calibration experiments, and assuming that the human finger is composed of two compounds, bone and soft tissue, it could be possible then to extract the soft tissue thickness, after calculating the percent of bone and tissue present in the measured site from equation (12):

$$Z_{eff} \text{ (total sample at incident energy } E_i \text{ and scattering angle } \Theta) = f_1 . Z_{eff\,(bone)} + f_2 . Z_{eff\,(soft\ tissue)} \qquad (12)$$

However, more work is required to fully address this new approach of soft tissue thickness. All normalization techniques tested above should correct for changes in flux and sample size. This was not tested as the phantoms were of constant size and the measurements for each setup were done on the same day, which meant the flux was constant for all measurements. As shown in literature, incoherent scatter normalization should also give information of the excitation source, sample size and position of the sample, and thus could be also used for signal normalization to correct for experimental variations.

In conclusion, previous Sr IVXRF studies avoided using incoherent scattering due to the difficulty in fitting the scatter peak. In these experiments, the incoming beam is monochromatic and the detection system comprises of a new multi-element collimated SDD carrying minimal electronic noise and having high energy resolution. The state of the art SDD detector and monochromatic x-ray tube yield the incoherent and coherent scatter peaks to be well separated with a rather low and flat background below them. Nevertheless, both incoherent scattering and coherent to incoherent scattering did not provide better signal normalization than the coherent scattering did alone. Consequently, the use of coherent to incoherent scatter ratio as an alternative correction for soft tissue thickness without the use of ultrasound imaging should be investigated. Further investigation of the exact relationship between the scatter ratio, and the effective atomic number is necessary to fully evaluate the use of coherent to incoherent scattering ratio for bone Sr IVXRF systems, both the source-based and the optically focused system.

Chapter 5 Conclusions and Future Work

5.1 Second Generation of the Diagnostic Tool for the *In vivo* Measurement of Strontium Levels in Human Bone

Sr is an element found naturally in the human body through food intake, where 99% of the total Sr body burden is present in bone (Nielson, 2004). Although Sr's therapeutic effect on bone health was first observed by Shorr and Carter in 1952, further studies regarding Sr's role in bone mineralization were overshadowed after the discovery of the presence of radioactive Sr-90 as a by-product of nuclear fissions from bomb testing. Nevertheless, three decades later, animal and human studies, along with the recent two large clinical trials, SOTI and TROPOS, have established the beneficial effects of administered Sr on bone formation and bone strength (Meunier *et al.*, 2009; Reginster *et al*., 2008). However, high levels of dietary Sr have been correlated with abnormal skeletal growth in animals and the incidence of rickets in children (Nielson, 2004; Özgür *et al.,* 1996). Therefore, one can conclude that Sr's effect on bone is dose dependent. On one hand, high doses of Sr results in hypomineralization and the deformation of the bone's crystal structure, inducing bone diseases; yet on the other hand, low doses of Sr improves bone strength and enhances bone mineralization.

The beneficial effects of Sr in bone warranted its use as a complimentary treatment for osteoporosis in the form of Sr Ranelate or Protelos®. However, because Sr has similar properties to Ca, it can interfere with the BMD values obtained from DEXA, the most common clinical diagnostic test for osteoporosis (Nielson *et al.,* 1999). Nielson and colleagues (1999) suggested a direct method to correct for the overestimated BMD values pertaining to patients taking Sr based supplements. This method however, relies on the knowledge of the absolute content of Sr in bone. Therefore, measuring Sr in bone is important first to differentiate between toxic and healthy levels and second, to correct for the false BMD values recorded from individuals taking Sr-based supplements, and thereby to monitor the progress of Sr based treatment of osteoporosis.

The two non-invasive x-ray techniques available to measure bone Sr are DPA and IVXRF. DPA is limited to measurement sites that can be immersed in a water bath to simulate soft tissue. More importantly, this technique is not sensitive enough to measure Sr levels in the population (Zamburlini *et al.*, 2008). The source-based Sr IVXRF system developed by our group is currently in clinical use to study the incorporation and retention of bone Sr after administration of Sr Citrate. The pilot study presently conducted demonstrated that the source based IVXRF system has enough sensitivity to monitor relative changes in bone Sr, however with a limited level of accuracy and precision. The accuracy of the source based system is limited by the polychromatic nature of the I-125 brachytherapy seeds, creating multiple overlapping x-ray and ϒ photon peaks. The poor energy resolution and slow peak shaping time of the Si(Li) detector used results in high dead times, typically 30-50% dead time for *in vivo* measurements, thus requiring an *in vivo* measurement to last at least 30 minutes real time. Moreover, using a radioactive isotope as the excitation source is rather inconvenient, since the source flux decreases with time and needs to be replaced regularly.

The optically focused IVXRF on the other hand, has the advantage that the excitation source is monochromatic and the exiting flux is relatively constant with time. Moreover, while accounting for the subject's effective dose, the higher source flux, dictated by the x-ray tube's voltage and current, can be exploited to shorten the measurement time. With a shorter measurement time, the subject tends to move less reducing the experimental error associated to an IVXRF measurement. In addition, repeated measurements are then possible, thus improving the precision. Furthermore, the x-ray beam size can be customized to the size of the subject's index finger by selecting the source to sample distance that best corresponds to the size of the finger. This option aims to reduce scattering from the overlying soft tissue and to possibly avoid exposing the subject to excess radiation that is not inducing Sr fluorescence.

The state of the art SDD complementing the optically focused x-ray tube, has a faster peak shaping time to tolerate high incoming count rates, while still producing characteristic and scatter x-ray peaks with superior energy resolution. The SDD detector's characteristic small size is advantageous, as it is Peltier cooled and thus does not require external liquid nitrogen; it is also is characterized by its minimum capacitance. Detectors with lower capacitance produce lower leakage currents and thus produce spectra having flat backgrounds (Lechner *et al*., 2004). This feature improves the accuracy of detecting and measuring Sr, especially in the case of *in vivo* measurements, where Compton scattering from tissue is significant.

Nevertheless, the most limiting factor of a bone Sr IVXRF measurement is the attenuation of Sr x-rays in soft tissue even after applying the analytical correction model developed by Zamburlini and colleagues (2007). This factor is one of the main hindrances for the bone Sr IVXRF system to be capable of extracting absolute [Sr]. Although the bulk of the work presented here does not fully address this issue, the second generation of the diagnostic tool was developed and optimized in hopes of improving the accuracy and precision of a Sr IVXRF measurement, along with establishing the preliminary facilitating steps toward extracting absolute Sr concentration. The latter is possible due to the simplicity of the system, where current numerical methods available to extract element concentration *in vitro* are facilitated when a monochromatic focused excitation source and a high energy resolution detector are used. Methods to quantify elemental concentration from *in vivo* measurements at the low energy range have yet to be developed.

5.1.1 Beam Imaging of the Optical System and Selection of Source to Sample Distance

The optically focused IVXRF system comprises of an x-ray tube based source and a detection system. The silver target x-ray tube is coupled with the DCC optics, which filters and focuses the out coming x-ray beam to produce mono-energetic Ag Kα x-rays with a beam spot size of 2.3 mm^2 at its focal length of 30 cm. At farther distances, the x-ray beam diverges to produce a beam spot of size 2.88 cm^2 at a source to sample distance of 101.5 cm. The two distances that produce a beam spot size comparable to the measurement site, the middle phalanx, are 70 and 78 cm from the tube. Both distances were shown to have the same sensitivity to detect Sr in bone phantoms demonstrated by their similar S/N ratio and detection limits (section 3.1). This was explained to be due to the fact that the beam spot size at 78 cm has a longer shape than the beam spot at 70 cm (table 2.1), thus activating a larger phantom area.

5.1.2 Selection of the Silicon Detector for the Optically Focused IVXRF System

The Zr collimated SDD was originally purchased for the optically focused IVXRF system to abide with the high incoming flux from the x-ray tube. The Zr collimated SDD was first tested with the I-125 brachytherapy seeds to compare its performance with the present source based system comprising of the Si(Li) detector and the I-125 brachytherapy seeds in 180° geometry. The Zr collimated SDD's superior resolution and faster peak shaping time (table 2.3) were overshadowed by its Zr contamination

interfering with the Sr K_β peaks and by its cutoff energy at 30 keV preventing coherent normalization. The direct MDLs obtained from both detectors with I- 125 brachytherapy seeds in backscatter geometry indicated that the Si(Li) detector outperformed the Zr collimated SDD.

Due to the aforementioned limitations of the Zr-collimated SDD, the detector was replaced by a new multi-element collimated SDD. The new multi-element SDD has an even better energy resolution than the former detector at the same peak shaping time and a P/B ratio, 15 times higher than the Zr collimated SDD (table 2.3). However the main two advantages of the multi-element collimated SDD over the Zr collimated SDD are the multi-element composition of the detector's collimator and the higher energy output range. The multi-element collimator restricts the fluorescence of a single element present in the detector to interfere with characteristic x-ray peaks originating from the sample, and the higher energy output range is useful for coherent normalization on the source-based system. However, when the multi-element collimated SDD was compared to the Si(Li) detector based on detection limits obtained when either detector was used with the optical system in 90° geometry at the same sample to detector and sample to source distance, the multi-element collimated SDD did not show superiority over the Si(Li) detector. After evaluating each detector's throughput with the Cd-109 excitation source and after comparing their absorption efficiencies at the Sr and Ag K x-ray energies, it was concluded that the Si(Li) detector detects Sr and Ag x-rays more efficiently than the multi-element collimated SDD under the same experimental conditions. On the other hand, it was shown in chapter 3 that the closer detector distance of 0.6 cm, possible with the multi-element SDD only, compensates for its smaller active area and slower throughput compared to the Si(Li) detector, thus resulting in reduced detection limits and a larger solid angle.

5.1.3 Investigation of Source-Phantom-Detector Geometry for the Optically Focused IVXRF System

In addition to investigating closer sample to detector distances, different source-phantom-detector geometries were investigated ranging from 90° to 152°. It was observed that at larger scattering angles, the sample to detector had to be positioned at a farther distance in order to prevent the detector's neck from intercepting the incoming x-ray beam. Therefore, spectra was collected and analyzed at a detector distance of 1 cm from the phantom instead. The Sr signal obtained was constant for all scattering angles except 152°. The reduced Sr, coherent, and Compton signal at this angle was explained to be due to some misalignment of the phantom with the detector at this angle. Further

experiments are recommended to confirm such a possibility. Nevertheless, the isotropic nature of the characteristic Sr x-ray at the rest of the scattering angles and the snapshots of the obtained spectra depicted in figures 3.3a) and 3.3b) suggests that 135° is a suitable angle for separating the scatter peaks, such that the closest sample to detector distance possible is then 0.8 cm. A full phantom calibration at 135° and at a detector distance of 0.8 cm is necessary to verify choosing this geometry.

In conclusion, whether a 90° or 135° geometry is adopted, the multi-element collimated SDD is the presently recommended silicon detector for bone Sr optically focused IVXRF, despite its small active area and poor absorption efficiency calculated in section 2.2.3. Finally, calculation of the detection limits obtained from all experiments did not include the uncertainties pertained to the calibration slope and intercept, which are not negligible. The reason was to follow the same calculation method used to determine MDLs for the source-based Sr IVXRF system, however future work should consider including them.

5.1.4 Sr Signal Normalization for the Optically Focused IVXRF System

The feasibility of Sr signal normalization by the Compton, coherent, and coherent/Compton scatter peaks was examined through theoretical and experimental approaches. Coherent normalization with the 35.5 keV coherent peak is used in the present source based bone Sr IVXRF system. This normalization has been adopted from the Pb Cd-109 source based IVXRF system, where the Pb x-ray to the Cd-109 ϒ photon ratio is independent of experimental factors such as source activity, subject positioning, subject's bone size, and subject's overlying soft tissue thickness (Somervaille *et al*., 1985). Although the conditions for coherent normalization described in section 4.1 are not strictly satisfied for bone Sr IVXRF, two feasibility tests were conducted: 1) the feasibility of using the coherent Ag Kα photons at 22.16 keV to correct the Sr signal for detector phantom positioning and 2) its feasibility to correct for the increasing tissue mimicking plastic thickness overlying the poP bone phantom. It was concluded that the Sr signal once normalized to the coherent Ag Kα signal, resulted in a ratio independent of varying the phantom to detector distances in the 90° geometry within 9.6% of the mean ratio. This is comparable to the obtained COV of 6.9% reported by Zamburlini *et al.* (2007). Moreover, the Sr/coherent ratios are not independent of varying tissue thickness, which is also in agreement with Zamburlini and colleagues (2007).

On the other hand, the conditions for normalizing the Sr signal with the Compton scatter peak set by Kalman and Heller (1962) and supported by the later works of Reynolds (1963) and Giauque (1979), to name a few, are all satisfied despite the majority of the analyzed samples being geological samples. As explained in section 4.2, for bone Sr IVXRF, Sr is a minor high Z element in a matrix that is mainly composed of light Z elements, thus its similarity to Sr in rocks. Experiments testing the feasibility of Compton normalization indicated that, similar to coherent normalization, the Sr/Compton ratio is invariant to changes in the sample to detector distance in 90° geometry within 22% of the mean ratio, while this ratio varied with changes in overlying soft tissue. The Compton normalized MDL obtained was found to be lower than the coherent normalized MDL (table 4.1) when the multi-element collimated SDD was positioned at a sample to detector distance of 0.6 cm in 90° geometry with respect to the source-phantom. The improved MDL after Compton normalization was explained to be due to the smaller relative uncertainty in the Compton peak area as opposed to that from the coherent peak area as the Compton peak is the dominant scatter peak with the present geometry.

Nevertheless, based on the feasibility experiments, the coherent normalization approach is recommended for the bone Sr optically focused IVXRF measurements.

The coherent to Compton ratio is widely included in quantitative XRF analysis for the determination of the absorption from light elements as well as sample thickness (Nielson, 1977). It has also been used to determine the effective number of a composite sample (Webster and Lilicrap, 1985). The use of this ratio for Sr signal normalization proved to be ineffective on both accounts, on correcting for changes in positioning and for changes in tissue thickness. Further optimizing the scatter peak fitting functions may however improve the relative error pertaining to the coherent scatter peak areas. Alternatively, building bone poP phantoms of different sizes and testing the efficacy of the coherent and the Compton scatter peak separately on correcting for the difference in bone size may result in a different conclusion. Therefore further testing is warranted to choose the more effective normalization approach.

In regards with compensating the inability for either proposed normalization to correct for Sr signal attenuation, determining the soft tissue thickness using ultrasound imaging is the approach presently used for the bone Sr source-based IVXRF system and should be used for the optically focused IVXRF system. An alternative approach has been proposed, where the ratio of the already available scatter peak areas, i.e. coherent to Compton peak, can be used to find the effective atomic number of the sample, which in turn can be used to extract the tissue thickness. However, this approach will

require further investigation and additional experiments to calibrate the coherent to Compton scatter peak with atomic number.

5.2 Future Work

5.2.1 Synthesis of New Bone Phantoms for the Calibration of the Bone Sr Optically Focused IVXRF System

The bone Sr calibration phantoms are cylindrical with a diameter of 7.5 mm, as mentioned in section 1.4. To prolong their life, they are placed inside a tissue mimicking plastic tube with 0.6 mm thickness. It is observed that exact positioning of the bone poP phantom with the source and detector to render 90° geometry is challenging with the phantoms inserted in the plastic tubes.

More importantly, the need to to synthesize new bone Sr phantoms has been discussed by Zamburlini (2008), Heirwegh (2008), and finally Moise (2010), since it is observed that the poP phantoms are contaminated with Sr before adding the known [Sr] to each phantom . This inherent contamination is apparent in the sample calibration line depicted in figure 1.1, where the intercept of the calibration line has a non-zero value. The level of contamination present in the poP phantoms can be evaluated by dividing the intercept of the calibration line to the slope of the calibration line. This value has been calculated to be around 400µg Sr/g Ca, which is problematic, since the level of Sr contamination is higher than the Sr level present in the skeleton of Reference Man (ICRP 23, 1975). This also means that Sr x-ray intensities corresponding to Sr levels below 400 µg Sr/g Ca, will result in negative [Sr], which is not realistic.

Therefore, building a new set of bone phantoms to better calibrate the system will reduce the uncertainty in the extracted [Sr] following an *in vivo* measurement, whether the source-based or the optically focused IVXRF system is used. The new bone phantoms should also improve the precision in reproducing the exact geometry and proper alignment of the bone and not the plastic tube with the optical system. The need for new bone phantoms for calibrating the both Sr IVXRF systems is being addressed by Eric Da Silva, who will be producing these phantoms with matrices based on hydroxyapatite. Hydroxyapatite based phantoms would have the same composition as human bone, which will relieve the necessity to correct for the difference in the coherent cross section between the

calibration standards and bone as discussed in section 4.1. The hydroxyapatite based phantoms are expected to be free of Sr contamination, thus allowing to extracting meaningful [Sr] following a bone Sr IVXRF measurement.

Sr is uniformly distributed through the hydroxyapatite matrix when Sr is ingested through diet (Dahl *et al.,* 2001). However, if Sr is administered regularly through Sr based supplements, Sr is observed to be preferentially deposited in the superficial layers of bone mineral (Dahl *et al.,* 2001). Therefore, the current Sr doped bone poP phantoms used to calibrate the Sr IVXRF system are not sufficient to correlate Sr x-ray intensities with [Sr] concentration in bone corresponding to subjects on a Sr supplement regime. One possible solution is to characterize the bone matrix of subjects administering Sr based supplements using Particle Induced X-ray Emission analysis, PIXE, *ex vivo,* to generate a Sr depth profile and correct for the non-uniform distribution of Sr in bone mineral. Alternatively, Gherase and colleagues (2009) proposed designing a multi-layered skin phantom of various arsenic (As) concentrations that are stacked together to better simulate the distribution of As in an individual's hand. The authors recommend this method only if the depth of the measured element's inhomogeneity is in the same order of the penetration depth of the fluorescent and incident x-rays in the given matrix. Applying this to bone Sr, Sr atoms should be distributed irregularly to a minimum depth of ~2.6cm. Thus PIXE would also be necessary to validate the use of multi-layered bone phantoms to calibrate the bone Sr optically focused IVXRF system for individuals under Sr medication.

Lastly, the source to sample distance was selected primarily to optimize the x-ray beam spot size with the area of the measured site for IVXRF measurements, the middle phalanx with a typical area of 1 cm^2, and not for the bare bone poP phantom measured area, which is 0.44 cm^2. In fact, for only the bone poP to be exposed and not the plastic tube, a source to sample distance close to 60 cm would be a better choice for phantom measurements (table 2.1). However, since the objective of this work is to optimize the optically focused IVXRF system for *in vivo* measurements, a new set of phantoms simulating the average size of an individual's finger bone is recommended. In addition, if a plastic tube is needed, it can be carved open on one side to restrict Sr and scatter x-rays from being attenuated before reaching the detector (figure 5.1).

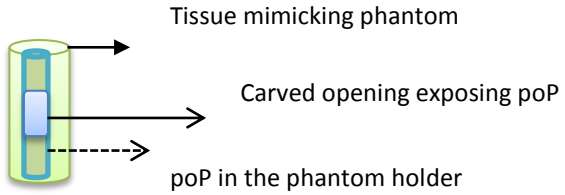

Figure 5.1: Schematic diagram depicting a tissue mimicking plastic housing the poP bone phantom. The tissue mimicking plastic has a window to expose the poP only.

5.2.2 Monitoring the Output Flux of the Optical System

Flux is defined as the number of photons emitted by the tube per unit area and per unit time. Calculating the output intensity or relative flux of the x-ray beam has the advantage of monitoring the optical system's stability on a day to day basis. The variation in the x-ray intensity has been questioned due to the large deviations in the fitted peak areas from one day's measurement to another. It would be useful to verify if indeed the output flux is fluctuating over time, or whether incorrect positioning of the poP bone phantom in the line of the x-ray beam is the reason for such deviations. Calculating the relative source intensity can be achieved by determining the detector's peak energy efficiency at the Ag Kα energy. The intrinsic peak energy efficiency is defined as the number of interactions that deposit the full energy of the incident radiation divided by the total number of quanta incident on the detector (Knoll's, 1989). This efficiency is insensitive to electronic noise and background scattering and is calculated by the following equation:

$$\varepsilon ip = \frac{4\pi \times \text{net count rate}}{emission\ probability \times source\ activity \times solid\ angle} \quad (1)$$

Determination of the intrinsic peak efficiency can be conducted using a Cd-109 radioactive source available in the laboratory, because Cd-109 decays to Ag-109 via electron capture and internal conversion resulting with a total emission probability of 100%. The net count rate in equation (1) is the number of counts under the Ag Kα peak divided by the live time. The solid angle is approximated as:

$$\Omega = \frac{\pi \times a^2}{d^2} \quad (2)$$

where "d" is the distance of the source from the detector and "a" is the radius of the detector. This approximation is valid since the detector's active area is much smaller than the source to detector distance. The source activity at the time of measurement should be corrected for photon attenuation from the source holder.

The intrinsic peak efficiency at a specific energy is characteristic to the detector, and thus once it is calculated for the Ag Kα x-ray energy, the above equation can be inversed to calculate the output flux. Therefore, a ten minute direct measurement of the optical system with the detector can monitor the output flux on a daily basis. The efficiency measurements of the Si(Li) detector and the multi-element

collimated SDD were performed with the Cd-109 radioactive source, yet the lack of information pertaining to the nature of the source holder and its thickness restricted the completion of these calculations.

5.2.3 Optimizing the X-ray Tube's Voltage and the Current Based on the Duration of a Measurement and Subject Dose

The x-ray tube was operated at a peak voltage of 40 kV and 40 mA for all the experiments discussed in this work. Although the x-ray tube's voltage is currently set at 80% its maximum value (50 keV) to prolong its life, the current can be raised to increase the output flux. A higher flux can be used to shorten the measurement time, where measurements can be repeated as well. Repeated measurements should improve the reproducibility of an IVXRF measurement. Varying the measurement time and voltage together should however be dictated by the patient's absorbed dose. Zamburlini and colleagues (2007) used LiF chips as dosimeters to measure the dose absorbed by the skin and finger bone from an *in vivo* measurement using the source-based IVXRF system. The resultant values were verified by Monte Carlo simulations, where the whole body effective dose from a 30 minute finger IVXRF measurement was determined to be 49.08 ± 0.05 nSv (Zamburlini *et al.,* 2007). The reported effective dose is equivalent to a three minute exposure to natural background in North America and thus, IVXRF is deemed harmless (Zamburlini *et al*., 2007). The x-ray tube produces a flux much higher than the I-125 brachytherapy seeds and thus a higher absorbed dose is expected. The x-ray beam from the optical system is more focused compared to a radioactive source, even at farther distances from the focal spot, this is advantageous not only for improving the system's sensitivity, but also for reducing the dose absorbed by the patient. Nevertheless, dosimetry measurements are imperative to verify such a hypothesis. In addition, these measurements are required to obtain ethics approval from Ryerson and McMaster University to conduct any future *in vivo* measurements.

5.2.4 Replacing the Multi-Element Collimated SDD with a Segmented SDD

Although the multi-element collimated SDD was selected as the better detector for Sr IVXRF, the SDD's high count rate capabilities were not exploited. That was explained to be due the low count rate at 90° geometry. Moreover, it was shown that phantom and detector positioning affected the precision of multiple measurements, which is also due to the difficulty in correctly positioning the detector and phantom to render 90° geometry.

An additional reason for the compromised reproducibility is the small active area of the multi-element collimated SDD. The majority of XRF applications that use SDD detectors require its fast processing of high input count rates, such as synchrotron based XRF analysis. High input count rates with enhanced energy resolution together are achievable only if the detector's active area is small (Lechner *et al.*, 2004). In fact, the largest commercially available SDD appears to have an active area of 100 mm^2, such as the Zr collimated SDD described in section 2.2. Coherent normalization and fixing the multi-element collimated SDD to the base of the shielding box was suggested to resolve or reduce the inaccurate positioning at either 135° or 90° geometry.

Alternatively, the multi-element SDD could be replaced by the later multi-array or segmented SDD. The segmented SDD is a continuous, gapless arrangement of a number of SDD's with an individual readout, but with a common voltage supply and entrance window (Lechner *et al.*, 2004). These emerging SDD's are advantageous, because they provide relatively large active areas and fast pulse processing without losing energy resolution of a single SDD cell. More importantly, the segmented SDDs can be structured to have their SDD cells in a donut like structure, where the incoming x-rays from the tube pass through the opening, thus creating the backscatter geometry (figure 5.2). As mentioned earlier, the backscatter or 180° geometry has been demonstrated to improve subject positioning and thus improve precision. An additional benefit of applying a 180° geometry setup is the minimum attenuation of the incident and exiting photons as the photons are normal to the tissue surface, compared to 90° geometry. The proposed arrangement of SDD cells and 180° geometry ensures that the incoming source photons from the optical system do not directly interact with the detector. This is not the case with the multi-element SDD placed in 90° with respect to the source and the phantoms as the proximity of the detector to the phantom was dictated by avoiding the beam to interact directly with the detector. Finally, in 180° geometry the input flux will be orders of magnitude higher than the current input flux at 90°, further improving the sensitivity and possibly allowing for shorter measurement times. Therefore, the segmented SDD should provide the many aforementioned advantages of designing the optically focused IVXRF system in the backscatter geometry, while maintaining the enhanced energy resolution. Backscatter geometry in conjunction with high pulse processing capabilities together should also improve the accuracy and precision of an *in vivo* measurement using the optically focused IVXRF. However, a new segmented SDD would be required to finally investigate these assumptions in the future.

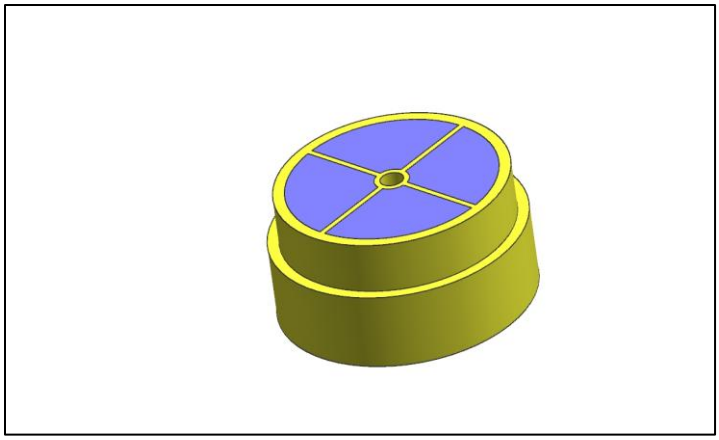

Figure 5.2: Side view of the segmental SDD detector head. The detector should be mounted on the optical system and the x-rays should pass through the opening in the centre.

References

Ahlgren, L., Liden, K., Mattsson, S., Tejning, S., Scand, J., (1976). X-ray fluorescence analysis of lead in human skeleton in vivo. *Scandinavian Journal of Work, Environment, and Health, 2, 82-86*.

Andermann, G., & Kemp, GW. (1958). Scattered X-Rays as Internal Standards in X-Ray Emission Spectroscopy. *Analytical Chemistry*, 30(8), 1306-1309

Berger, M.J., Hubbell, J.H., Seltzer, S.M., Chang, J., Coursey, J.S., Sukumar, R., Zucker,. D.S. (2005). XCOM: Photon Cross Section Database (version 1.3) (Gaithersburg, MD: National Institute of Standards and Technology) http://physics.nist.gov/xcom

Bevington, P. R. (1969). *Data reduction and error analysis for the physical sciences*. New York: McGraw Hill

Boivin, G., Farlay, D., Khebbab, M., Jaurand, X., Delmas, P., & Meunier, P. (2010). In osteoporotic women treated with strontium ranelate, strontium is located in bone formed during treatment with a maintained degree of mineralization. *Osteoporosis International, 21*(4), 667-677.

Buehler, J., Chappuis, P., Saffar, J. L., Tsouderos, Y., & Vignery, A. (2001). Strontium ranelate inhibits bone resorption while maintaining bone formation in alveolar bone in monkeys (macaca fascicularis). *Bone, 29*(2), 176-179

Byun, S. H., Pejović-Milić, A., McMaster, S., Matysiak, W., Aslam, , Liu, Z., . . . Chettle, D. R. (2007). Dosimetric characterization of the irradiation cavity for accelerator-based in vivo neutron activation analysis. *Physics in Medicine and Biology, 52*(6), 1693-1703.

Cabrera, W.E., Schrooten, I., De Broe, ME., D'Haese, PC,. (1999). Strontium and bone. *J. Bone Miner. Res.*, 14 (5): 661-668

Chettle, D. R., Scott, M. C., & Somervaille, L. J. (1989). Improvements in the precision of in vivo bone lead measurements. *Physics in Medicine and Biology, 34*(9)

Chen, Z.W., Gibson, W.M., Huang, H. (2008). High Definition X-Ray Fluorescence: Principles and Techniques. *X-Ray Optics and Instrumentation*

Comar CL, Russell RS, Wasserman RH. (1957). Strontium-calcium movement from soil to man. Science. 126 (3272), 485-492

Donativi, M., Quarta, S., Cesareo, R., & Castellano, A. (2007). Rayleigh to compton ratio with monochromatic radiation from an X-ray tube (preliminary results). *Nuclear Inst. and Methods in Physics Research, B, 264*(1), 189-193

Duvauchelle, P., Peix, G., & Babot, D. (1999). Effective atomic number in the rayleigh to compton scattering ratio. *Nuclear Instruments and Methods in Physics Research Section B: Beam Interactions with Materials and Atoms, 155*(3), 221-228

Firestone, LBNL Isotopes Project Nuclear Data Dissemination Home Page, Ernest Orlando Lawrence Berkeley National Laboratory:Berkeley, 2005, http://ie.lbl.gov/toi.html.

Ferraro, E.F., Carr, R., Zimmerman, K. (1983). A comparison of the effects of strontium chloride and calcium chloride on alveolar bone. *Calcified Tissue International*, 35, 258-260

Fonseca, J. E. (2008). Rebalancing bone turnover in favour of formation with strontium ranelate: Implications for bone strength. *Rheumatology, 47*, iv17-iv19

Gherase, M. R., & Fleming, D. E. B. (2009) K-shell X-ray fluorescence measurements of arsenic depth-dependent concentration in polyester resin discs using the fundamental parameter method. *Applied Radiation and Isotopes, 67*(1), 50-54

Giauque, R.D., Garrett, R.B., Goda, L.Y. (1979). Determination of trace elements in light element matrices by x-ray fluorescence spectrometry with incoherent scattered radiation as an internal standard. *Analytical Chemistry*, 51(4), 511-516

Grynpas, M. D., Hamilton, E., Cheung, R., Tsouderos, Y., Deloffre, P., Hott, M., & Marie, P. J. (1996). Strontium increases vertebral bone volume in rats at a low dose that does not induce detectable mineralization defect. *Bone, 18*(3), 253-259.

Heirwegh, C. (2008). *IN VIVO QUANTIFICATION OF BONE STRONTIUM USING X-RAY FLUORESCENCE*, M.Sc. Thesis. McMaster University

Hower, J. (1959). Matrix corrections in x-ray spectrographic trace element analysis of rocks and minerals. *American Mineralogy,* 44, 19-29

Hult, M., Fessler, A., (1998). Sr/Ca mass ratio determination in bones using fast neutron activation analysis. *Applied Radiation and Isotopes,* 49, 1319–132

International Commission on Radiological Protection (ICRP) (1975). Report of the Task Group on Reference Man *ICRP Publication 23* (Oxford: Pergamon)

International Commission on Radiological Protection (ICRP) (1993). Age-Dependent Doses to Members of the Public from Intake of Radionuclides *ICRP Publication 67* (Oxford: Pergamon)

International Commssion on Radiological Protection (ICRP) (1995). Basic Anatomical and Physiological Data for the use in Radiological Protection: the Skeleton *ICRP publication 70* (Oxford: Pergamon)

Kendler, D., Adachi, J., Josse, R., & Slosman, D. (2009). Monitoring strontium ranelate therapy in patients with osteoporosis. *Osteoporosis International, 20*(7), 1101-1106

Kerr, S. A., Kouris, K., Webber, C. E., & Kennett, T. J. (1980). Coherent scattering and the assessment of mineral concentration in trabecular bone. *Physics in Medicine and Biology, 25*(6), 1037-1047.

Kalman, Z.H., & Heller, L. (1962). Theoretical Study of X-Ray Fluorescent Determination of Traces of Heavy Elements in a Light Matrix: Application to Rocks and Soils. *Analytical Chemistry,* 34 (8), 946-951

Knoll, G. F. (1989). *Radiation detection and measurement*. New York: John Wiley and Sons.

Leoni, L., & Saitta, M. (1977). Matrix effect corrections by Ag Kα Compton scattered radiation in the analysis of rock samples for trace elements. *X-Ray Spectrometry,* 6, 181–186

Lechner, P., Fiorini, C., Hartmann, R., Kemmer, J., Krause, N., Leutenegger, P., . . . Weber, U. (2001). Silicon drift detectors for high count rate X-ray spectroscopy at room temperature. *Nuclear Instruments and Methods in Physics Research Section A: Accelerators, Spectrometers, Detectors and Associated Equipment, 458*(1-2), 281-287

Lechner, P., Pahlke, A., & Soltau, H. (2004). Novel high-resolution silicon drift detectors. *X-Ray Spectrometry, 33*(4), 256-261

Marie, P.J., Garba, M.T., Hott, M.L., Miravet, L. (1985). Effect of low doses of stable strontium on bone metabolism in rats. *Mineral Electrolyte Metabolism,* **11**, 5-13

Marie, P. J., Ammann, P., Boivin, G., & Rey, C. (2001). Mechanisms of action and therapeutic potential of strontium in bone. *Calcified Tissue International, 69*(3), 121-129.

McCaslin, F. E., & Janes, H. M. (1959). The effect of strontium lactate in the treatment of osteoporosis. *Mayo Clinic Proceedings, 34*, 329-334.

Meunier, P., Roux, C., Ortolani, S., Diaz-Curiel, M., Compston, J., Marquis, P., . . . Reginster, J. (2009). Effects of long-term strontium ranelate treatment on vertebral fracture risk in postmenopausal women with osteoporosis. *Osteoporosis International, 20*(10), 1663-1673

Moise, H. (2010). *IN VIVO MEASUREMENT OF STRONTIUM INCORPORATION AND RETENTION IN HUMAN BONE USING AN X-RAY FLUORESCENCE SYSTEM*, M.Sc. Thesis. Ryerson University.

Nielson KK. (1977). Matrix corrections for energy dispersive x-ray fluorescence analysis of environmental samples with coherent/incoherent scattered x-rays. Analytical Chemistry, 49 (4), 641-648

Nielsen, S. P., Slosman, D., Sorensen, O. H., Basse-Cathalinat, B., De Cassin, P., Roux, C., & Meunier, P. J. (1999). Influence of strontium on bone mineral density and bone mineral content measurements by dual X-ray absorptiometry. *Journal of Clinical Densitometry, 2*(4), 371-379.

Nielsen, S. P., Barenholdt, O., Barenholdt-Schioler, C., Mauras, Y., & Allain, P. (2004). Noninvasive measurement of bone strontium. *Journal of Clinical Densitometry, 7*(3), 262-268.

Nielsen, S.P. (2004). The biological role of strontium. *Bone, 35*(3), 583-588.

O'Meara, J. M., Chettle, D. R., McNeill, F. E., & Webber, C. E. (1997). The feasibility of measuring bone uranium concentrations in vivo using source excited K x-ray fluorescence. *Physics in Medicine and Biology, 42*(6), 1109-1120

O'Meara, J.M., Borjesson, J., Chettle, D.R., Mattsson, S. (2001). Normalisation with coherent scatter signal: improvements in the calibration procedure of the Co-57-based in vivo XRF bone-Pb measurement. *Applied Radiation and Isotopes***,** 54 (2), 319-325.

Özgür, S., Sümer, H., Koçoğlu, G. (1996). Rickets and soil strontium. *Archives of Disease in Children,* 75, 524-526.

Pejović-Milić, A., Brito, J.A., Gyorffy, J., Chettle, D.R. (2002). Ultrasound measurements of overlying soft tissue thickness at four skeletal sites suitable for *in-vivo* x-ray fluorescence. *Journal of Medical Physics*, 29 (11), 2687-2691.

Pejović-Milić, A., Stronach, I.M., Gyorffy, J., Webber, C.E., Chettle, D.R. (2004). Quantification of bone strontium levels in humans by in vivo x-ray fluorescence. *Journal of Medical Physics,* 31 (3), 528-538.

Pejović-Milić, A. (2001*). IN VIVO MEASUREMENTS OF ALUMINUM AND STRONTIUM IN HUMAN BONE*. Ph.D. Dissertation. McMaster University

Register JY, Seeman E, De Vernejoul MC, Adami S, Compston J, Phenekos C, Devogelaer JP, Curiel MD, Sawicki A, Goemaere S, Sorensen OH, Felsenberg D, Meunier PJ (2005) Strontium ranelate reduces the risk of nonvertebral fractures in postmenopausal women with osteoporosis: Treatment of Peripheral Osteoporosis (TROPOS) study. *Journal of Clinical Endocrinology and Metabolism,* 90 (5), 2816-2822.

Riggs, B. L., & Parfitt, A. M. (2005). Drugs Used to Treat Osteoporosis: The Critical Need for a Uniform Nomenclature Based on Their Action on Bone Remodeling. *Journal of Bone and Mineral Research*, 20, 177–184.

Ryan, E. A., & Farquharson, M. J. (2010). The differentiation between malignant and non-malignant breast tissues using elastic and inelastic scattering of synchrotron radiation. *Nuclear Inst. and Methods in Physics Research, A, 619*(1-3), 379-384

Reynolds, R.C. (1963). Matrix correction in trace element analysis by x-ray fluorescence: estimation of the mass absorption coefficient by Compton scattering. *American Mineralogy*, 48, 1133–1143

Robinson, R. G., Blake, G. M., McEwan, A. J., Spicer, J. A., & Martin, N. L. (1989). Strontium-89: Treatment results and kinetics in patients with painful metastatic prostate and breast cancer in bone. *Radiographics, 9*(2), 271-282.

Shorr, E., & Carter, A.C. (1952). *Bulletin of the Hospital for Joint Diseases,* 13, 59.

Sitko, R. (2006). Correction of matrix effects via scattered radiation in X-ray fluorescence analysis of samples collected on membrane filters. *Journal of Analytical Atomic Spectrometry*, 21, 1062-1067

Snyder, R. E., & Secord, D. C. (1982). The in situ measurement of strontium content in bone using X-ray fluorescence analysis. *Physics in Medicine and Biology, 27*(4), 515-529

Somervaille, L.J., Chettle, D.R., Scott, M.C. (1985). *In vivo* measurement of lead in bone using x-ray-fluorescence. *Physics in Medicine and Biology,* 30**,** 929–943.

Sutcliffe, J. F. (1996). A review of in vivo experimental methods to determine the composition of the human body. *Physics in Medicine and Biology, 41*(5), 791-833.

Tertian, R., Claisse, F. (1982). The scattered radiation method. In *Principles of quantitative X-ray fluorescence analysis* (pp. 258-277). London: Heyden and Sons Ltd.

Turekian, K.K. & Kulp, J.L. (1956). Strontium content of human bones. *Science,* 124 (3218), 405-407

Turekian, K.K. & Wedepohl, K.H. (1961). Distribution of elements in some major units of the earth's crust. *Geological Society of America*, 72, 175-192

Todd, A. C. (2000). Coherent scattering and matrix correction in bone-lead measurements. *Physics in Medicine and Biology, 45*(7), 1953-1963.

Wielopolski, L., Vartsky, D., Yasumura, S., Cohn, S.H. (1983). Application of XRF to measure strontium in human bone *in vivo*. *Advances in X-ray Analysis,* 26, 415-421

WHO. (1994). *Study Group on Assessment of Fracture Risk and its Application to Screening for Postmenopausal Osteoporosis*. *Technical Report Series (World Health Organization).* WHO, Geneva.

Verberckmoes, S. C., De Broe, M. E., & D'Haese, P. C. (2003). Dose-dependent effects of strontium on osteoblast function and mineralization. *Kidney International, 64*(2), 534-543

Verdurmen, E. A. (1977). Accuracy of X-ray fluorescence spectrometric determination of rb and sr concentrations in rock samples. *X-Ray Spectrometry, 6*(3), 117-122.

Webber, C. E. (2006). Photon absorptiometry, bone densitometry and the challenge of osteoporosis. *Physics in Medicine and Biology, 51*(13), R169-R185

Webster, D. J., & Lillicrap, S. C. (1985). Coherent-compton scattering for the assessment of bone mineral content using heavily filtered X-ray beams. *Physics in Medicine and Biology, 30*(6), 531-539

Zaichick, V. (2006). INAA of ca, cl, K, mg, mn, na, P, and sr contents in the human cortical and trabecular bone. *Journal of Radioanalytical and Nuclear Chemistry, 269*(3), 653-659

Zamburlini, M., Pejović-Milić, A., & Chettle, D. R. (2006). Evaluation of geometries appropriate for 125I in vivo bone strontium X-ray fluorescence measurement. *Journal of Radioanalytical and Nuclear Chemistry, 269*(3), 625-629

Zamburlini, M., Pejović-Milić, A., Chettle, D. R., Webber, C. E., & Gyorffy, J. (2007). In vivo study of an x-ray fluorescence system to detect bone strontium non-invasively. *Physics in Medicine and Biology, 52*(8), 2107-2122

Zamburlini, M., Pejović-Milić, A., & Chettle, D. R. (2008). Coherent normalization of finger strontium XRF measurements: Feasibility and limitations. *Physics in Medicine and Biology, 53*(15), N307-N313

Zamburlini, M. (2008). *IN VIVO MEASUREMENT OF BONE STRONTIUM WITH X-RAY FLUORESCENCE*, Ph.D. Dissertation. McMaster University.

Zamburlini, M., Pejović-Milić, A., & Chettle, D. R. (2008). Spectrometry methods for in vivo bone strontium measurements. *X-Ray Spectrometry, 37*(1), 42-50